UNIVERSITÉ DU QUÉBEC À MONTRÉAL

ÉVALUATION DES NUAGES ET DE LEUR INTERACTION AVEC LE RAYONNEMENT DANS LE MODÈLE GEM

MÉMOIRE

PRÉSENTÉ

COMME EXIGENCE PARTIELLE

DE LA MAÎTRISE EN SCIENCES DE L'ATMOSPHÈRE

PAR

DANAHÉ PAQUIN-RICARD

JANVIER 2009

REMERCIEMENTS

Je tiens à remercier mes directeur et co-directeur, Colin Jones et Paul Vaillancourt, pour leur soutien et leur aide tout au long de ma maîtrise et plus particulièrement mon directeur pour ses bons conseils, sa patience et ses encouragements lors de la rédaction de l'article. Je tiens aussi à remercier mes collègues de bureau qui, à tous les jours, rendent l'environnement de travail stimulant et qui sont toujours disponibles pour offrir leur aide et leur soutien moral. Finalement, je remercie mon copain pour toute sa patience, son soutien et son enthousiasme envers mes projets de recherche.

TABLE DES MATIÈRES

LISTE DES FIGURES

LISTE DES TABLEAUX

LISTE DES ABRÉVIATIONS, SIGLES ET ACRONYMES

ARM	Atmospheric Radiation Measurement
CF	Cloud Fraction
CKD	Correlated K-Distribution
DJF	December-January-February
ECMWF	European Centre for Medium-Range Weather Forecasts
ERA40	ECMWF Reanalysis
GEM	Global Environmental Multi-scale Model
GEM-LAM	Global Environmental Multi-scale Limited-Area Model
GIEC	Groupe d'experts Intergouvernemental sur l'Evolution du Climat
GCM	Global Climate Model
Had-GEM	Hadley center Global Environmental Model
IPCC	Intergovernmental Panel on Climate Change
ISCCP	International Satellite Cloud Climatology Project
IWP	Ice Water Path
IWV	Integrated Water Vapor
IPCC	Intergovernmental Panel on Climate Change
JJA	June-July-August
LBC	Lateral Boundary Condition
LWD	Downwelling Longwave radiation
LWP	Liquid Water Path
NCAR-CCM3	National Center for Atmospheric Research Community Climate Model version 3
NSA	North Slope of Alaska
RCM	Regional Climate Model
SCM	Single-Column Model

SGP	Southern Great Plains
SRB	Surface Radiation Budget
SST	Sea Surface Temperature
SWD	Downwelling Shortwave radiation
SZA	Solar Zenith Angle
TKE	Turbulent Kinetic Energy
TOTWP	Total Water Path

RÉSUMÉ

Cette étude se penche sur l'interaction nuage-rayonnement simulée par le modèle GEM-LAM (modèle Global Environnemental Multi-échelle à aire limitée) en évaluant avec des observations provenant de deux sites du programme ARM (Atmospheric Radiation Measurement) les différentes composantes atmosphériques ayant un impact sur le bilan radiatif de surface. Ainsi, le rayonnement vers la surface de courtes et longues longueurs d'ondes est comparé aux observations en fonction de la fraction nuageuse afin d'isoler l'effet de la vapeur d'eau ou de l'eau liquide des nuages sur le rayonnement descendant. À l'aide des cycles diurnes moyens et des distributions de fréquences, le principal biais identifié pour le rayonnement à la surface simulé par GEM-LAM est la surestimation du rayonnement d'ondes courtes incident à la surface vers le milieu de la journée. Ce biais provient, d'une part, d'une sous-estimation de la fraction nuageuse, et d'autre part, d'une trop grande transmissivité du rayonnement solaire des nuages lorsqu'ils sont présents, particulièrement pour les nuages optiquement minces. Le biais radiatif de courtes longueurs d'ondes est responsable d'un biais chaud de température près de la surface pour les saisons d'été aux deux sites. Ceci entraîne un biais positif du rayonnement d'ondes longues pour les conditions de ciel clair qui est toutefois compensé par la sous-estimation de la fraction nuageuse pour donner des biais réduits du rayonnement d'ondes longues pour toutes les conditions. De plus, le biais de courtes longueurs d'ondes pourrait être responsable d'un assèchement excessif de la surface et par conséquent mener à un déficit de vapeur d'eau dans l'atmosphère, particulièrement pour la saison d'été au site SGP. Cette étude illustre l'importance de l'évaluation individuelle des composantes de l'interaction nuage-rayonnement à l'aide de statistiques à hautes fréquences temporelles afin de bien identifier les erreurs compensatoires qui peuvent être présentes.

Mots clés : interaction nuage-rayonnement, modèle régional de climat, schéma microphysique, bilan radiatif de surface

INTRODUCTION

La modélisation du climat a pour but de comprendre, reproduire et projeter le climat passé, présent et futur. L'augmentation de la capacité de calcul des ordinateurs a permis un développement des modèles climatiques d'une part en augmentant leur résolution spatio-temporelle et d'autre part en permettant l'inclusion d'un plus grand nombre de processus influençant le climat ou la complexification de ceux déjà inclus. Avec ces nouvelles possibilités, une attention particulière est portée à l'amélioration du réalisme physique des paramétrages inclus dans les modèles climatiques.

Selon le GIEC (Groupe d'Experts Intergouvernemental sur l'Évolution du Climat, Randall et al. (2007)), les différences entre les modèles climatiques quant à la simulation des rétroactions des nuages (qui se font notamment par l'interaction nuages-rayonnement) est la principale source de l'étalage intermodèle de l'estimé de la sensibilité climatique. De plus, les évaluations basées sur les observations de ces rétroactions montrent que les différents modèles climatiques ont différentes forces et faiblesses et qu'il n'est pas toujours possible de déterminer quelles projections futures de ces rétroactions sont les plus fiables. Ainsi, les rétroactions des nuages sur le système climatique sont considérées comme une source importante d'incertitude dans les projections climatiques (Stephens (2005)).

L'interaction nuage-rayonnement est une composante importante des rétroactions possibles des nuages sur le système climatique puisqu'elle contrôle notamment le bilan radiatif de surface. En effet, outre les caractéristiques de la surface qui déterminent le rayonnement d'ondes courtes réfléchi vers le haut ainsi que le rayonnement d'ondes longues absorbé et émis, le rayonnement qui atteint la surface (vers le bas) dépend de la composition de l'atmosphère. Ainsi, le rayonnement peut être transmis, réfléchi, diffusé, absorbé et réémis par le contenu en eau de l'atmosphère (sous ses trois phases), les

différents gaz ou aérosols présents. La présence de nuages et leur composition peuvent alors modifier le bilan radiatif de surface, ce qui a un impact sur les processus de surface tels que la fonte du couvert de neige et l'évaporation, qui en retour peuvent influencer la formation des nuages. Cette interaction peut donc mener à plusieurs rétroactions dans le système climatique.

L'interaction nuage-rayonnement est définie comme un ensemble de processus impliquant diverses échelles spatio-temporelles puisqu'elle dépend à la fois de la microphysique des nuages, de leurs caractéristiques macroscopiques et de leur environnement. Les processus microphysiques des nuages contrôlent l'évolution temporelle du contenu en eau (liquide et solide) du nuage, ses distributions spatiale et de taille et la production de la précipitation. Les caractéristiques macroscopiques des nuages comprennent leur géométrie, hauteur, extension verticale, température et position les uns par rapport aux autres. Finalement, l'environnement comprend, entre autres, la vapeur d'eau, les autres gaz et les aérosols présents dans l'atmosphère au-dessous et au-dessus du nuage, le profil thermodynamique ainsi que la dynamique atmosphérique.

Dans les modèles de climat, l'effet des nuages sur le rayonnement doit être paramétré puisqu'un grand nombre des processus impliqués ne sont pas résolus dans le modèle (processus sous-maille). Cette paramétrisation implique à la fois le schéma microphysique qui représente les caractéristiques sous-maille d'un nuage modélisé et à la fois le schéma de transfert radiatif qui calcule l'absorption, la transmission, la réflection, la diffusion et l'émission du rayonnement en fonction des divers composés présents dans la colonne atmosphérique et qui sont spécifiés soit par le schéma microphysique pour ce qui concerne l'eau sous toutes ses phases, soit par d'autres paramétrages pour ce qui est des gaz rares et des aérosols. Selon la résolution des modèles, certains nuages de grandes tailles peuvent être résolus mais leurs processus internes, qui sont de sous-échelle, doivent être paramétrés. Différentes complexités de schémas microphysiques sont aujourd'hui utilisées dans les modèles climatiques, allant des paramétrisations qui ne comprennent qu'une seule variable pronostique pour le contenu total en eau du nuage aux paramétrages à multiples moments (i. e. le rapport de mélange, la concentration)

qui peuvent comprendre plusieurs variables pronostiques pour représenter les différents types d'hydrométéores.

Plusieurs études se sont déjà penchées sur l'évaluation des nuages dans les modèles climatiques ainsi que les erreurs que ceux-ci entraînent sur le bilan radiatif. Parmi ces études, certaines sont faites avec un modèle de circulation globale (Cess et Coauthors (1996) ; Norris et Weaver (2001) ; Walsh et al. (2002) ; Weare (2004) ; Martin et al. (2006) ; Williams et al. (2006)), ce qui permet d'évaluer à la fois la simulation directe des nuages et à la fois leurs rétroactions avec le système climatique simulé. D'autres auteurs ont utilisé les modèles colonnes (Curry et Coauthors (2000) ; Iacobellis et al. (2003) ; Lenderink et al. (2004) ; Yuan et al. (2006)) qui permettent de prescrire directement les paramètres dynamiques et thermodynamiques au modèle afin de s'assurer de faire une évaluation des nuages simulés dans des conditions très similaires aux données d'observations. Finalement, une troisième catégorie de modèles est utilisée, soit les modèles régionaux du climat (Roads et al. (2003) ; Meinke (2006) ; Willén et al. (2005) ; Morrison et Pinto (2006) ; Markovic et al. (2008) ; Wyser et al. (2008) ; Tjernström et al. (2008)) qui permettent, par un bon choix de conditions aux frontières latérales, de prescrire de grandes échelles semblables aux observations mais qui laissent place au développement de rétroactions par les nuages simulés dans les plus petites échelles (Hogan et al. (2001) ; van Meijgaard et Crewell (2005)).

Ainsi, Norris et Weaver (2001) ont comparé les propriétés des nuages simulées par le modèle NCAR-CCM3 (National Center for Atmospheric Research Community Climate Model version 3) à plusieurs observations au-dessus de l'océan Pacifique Nord en été. Leur analyse montre que des erreurs dans la paramétrisation des petites échelles des nuages mène à une variabilité des propriétés nuageuses (telles que la couverture nuageuse, le forçage radiatif ou l'épaisseur optique des nuages) incorrecte malgré une bonne climatologie des nuages simulés. Ceci peut donc résulter en des rétroactions des nuages erronnées particulièrement lors de projections de changements climatiques. Par la suite, Martin et al. (2006) ont présenté une évaluation de la climatologie mondiale du modèle HadGEM (Hadley Centre Global Environmental Model) après des modi-

fications au schéma microphysique. Avec ce nouveau schéma basé sur la distribution de taille avec une variable pronostique supplémentaire pour la glace, ils ont noté des améliorations importantes dans la représentation des nuages par rapport à l'ancienne version. Ils ont pu démontrer une amélioration cohérente entre les nuages et les flux radiatifs puisque le modèle, en simulant mieux les différents types de nuages (comparés aux observations), a produit un bilan radiatif au sommet de l'atmosphère plus près des observations. Récemment, Markovic et al. (2008) ont évalué trois modèles régionaux au-dessus de l'Amérique du Nord avec des observations de surface. Ils ont trouvé que les erreurs de fraction nuageuse et de rayonnement d'ondes courtes en ciel clair (sans nuage) se compensent souvent pour résulter en un rayonnement d'onde courte plus près des observations lorsque tous les cas sont analysés ensemble (indépendemment de la fraction nuageuse). Wyser et al. (2008) et Tjernström et al. (2008), ont quant à eux, évalués plusieurs modèles régionaux au-dessus de l'Arctique avec des observations et ils ont trouvé que la plupart des modèles n'arrivent pas à bien reproduire le cycle annuel de la fraction nuageuse observée. Ils concluent qu'une amélioration de la paramétrisation de la fraction nuageuse et de la microphysique des nuages de phase mixte est requise pour améliorer la performance générale des modèles régionaux au-dessus de l'Arctique. Finalement, Morrison et Pinto (2006) suggèrent que certains paramètres présents dans les schémas microphysiques plus simples des modèles climatiques sont basés sur des observations faites aux latitudes moyennes et qu'ils ne sont donc pas appropriés pour la simulation des nuages en Arctique.

Cette étude se concentre sur l'évaluation de l'interaction nuage-rayonnement dans le modèle GEM version 3.2.2 (Côté et al. (1998)). La version à aire limitée du modèle (GEM-LAM), qui sera la prochaine version du modèle régional canadien du climat (Zadra et al. (2008)), a été choisie puisqu'elle offre un compromis entre un modèle mondial et un modèle colonne quant à l'évaluation simultannée des nuages simulés et de leurs rétroactions sur le système climatique simulé. Cette étude est présentée sous forme d'article rédigé avec l'aide de mes directeur et co-directeur et qui a été soumis à la revue *Monthly Weather Review*. Le modèle GEM-LAM possède un schéma microphysique de

type *bulk* avec une seule variable pronostique pour l'eau totale des nuages non-convectifs et la fraction nuageuse est basée sur une approche du seuil d'humidité relative (Sundqvist (1988)). Le schéma de transfert radiatif provient de Li et Barker (2005) et utilise la méthode de la distribution-k corrélée.

Deux simulations avec une résolution horizontale de 0.5 ° ont été faites au-dessus de deux domaines différents, chacun centré sur un site d'observations du programme ARM (Atmospheric Radiation Measurement). Les simulations de sept à huit années ont été exécutées avec les conditions aux frontières latérales provenant des réanalyses ERA-40 (Uppala et al. (2005)). Le choix des deux sites d'observations est dû aux climats radicalement différents qui y prévalent afin de tester les capacités du modèle à bien représenter l'interaction nuage-rayonnement lorsque différents processus microphysiques, thermodynamiques et dynamiques ont cours. L'évaluation porte donc sur ces deux sites pour les saisons d'été et d'hiver. Les principales variables analysées, en plus de la fraction nuageuse et du rayonnement à la surface de courtes et longues longueurs d'ondes (CF, SWD et LWD respectivement), sont la vapeur d'eau et l'eau liquide intégrées à la verticale (IWV et LWP), la précipitation et la température près de la surface.

Plusieurs outils d'analyse sont utilisés afin de cerner les erreurs qui pourraient contribuer au bilan radiatif de surface. Les cycles diurnes moyennés par saison comparent les sorties du modèle et les observations moyennées aux trois heures afin d'identifier les compensations possibles dans le temps. Les distributions de fréquences sont utilisées pour comparer les quantités telles que la précipitation ou l'eau liquide des nuages afin de vérifier que la moyenne simulée de ces quantités ne provient pas de compensations entre différents régimes. De plus, des graphiques de co-variabilité entre le rayonnement et la vapeur d'eau ou l'eau liquide sont utilisés afin de comparer la relation entre ces quantités dans le modèle et dans les observations. Une séparation est aussi faite en fonction de la fraction nuageuse afin d'isoler les effets de la vapeur d'eau (ainsi que les gaz rares et les aérosols présents) de l'effet de l'eau condensée des nuages en émettant l'hypothèse que pour une fraction nuageuse de 10 % et moins, les effets de l'eau condensée sont négligeables alors que pour une fraction nuageuse de 90 % et plus, les effets de l'eau

condensée dominent par rapport à ceux de la vapeur d'eau.

CHAPITRE I

ARTICLE

Using ARM observations to evaluate cloud and clear-sky radiation processes as simulated by the Canadian regional climate model GEM.

Danahé Paquin-Ricard
Université du Québec à Montréal, Montréal, Canada

Colin Jones
Rossby Centre, Swedish Meteorological and Hydrological Institute, Norrköping, Sweden

Paul A. Vaillancourt
Rcchcrche en Prévisions Numériques, Meteorological Research Division, Dorval, Canada

Soumis à la revue *Monthly Weather Review* (28 juillet 2008)

ABSTRACT

The total downwelling shortwave (SWD) and longwave (LWD) radiation and its components are assessed for the limited-area version of the Global Environmental Multi-scale model (GEM-LAM) against ARM observations at two sites, Southern Great Plains (SGP) and North Slope of Alaska (NSA) for the period 1998-2005. Model and observed SWD and LWD are evaluated as a function of cloud fraction (CF), i.e. for overcast and clear-sky conditions separately, to isolate and analyze different interactions between radiation and (1) atmospheric aerosols and water vapor and (2) cloud liquid water. Through analysis of the mean diurnal cycle and normalized frequency distributions of surface radiation fluxes, the primary radiation error in GEM-LAM is seen to be excess SWD in the middle of the day. This leads to the development of a warm near-surface temperature bias, particularly during summer at both sites. The SWD bias results from a combination of underestimated CF and clouds, when present, possessing too high solar transmissivity, this being particularly the case for optically thin clouds. The warm bias is the primary cause of excess clear-sky LWD. This excess is partially balanced with respect to the all-sky LWD by an underestimated CF, which causes a negative bias in simulated all-sky emissivity. The excess SWD may also lead to a surface dry bias and contribute to a negative bias in IWV, particularly at SGP in the summer. It is shown that there is strong interaction between all the components influencing the simulated surface radiation fluxes with frequent error compensation, emphasizing the need to evaluate the individual radiation components at high time frequency.

1.1 Introduction

The surface radiation budget (SRB) is one of the main controls on key surface variables such as temperature, soil moisture, snow cover and evaporation rates. A systematic bias in the simulated SRB can lead to errors in any of these variables, with the potential for subsequent error propagation throughout the simulated climate system. With respect to simulating anthropogenic climate change and feedbacks involving cloud-radiation interactions, it is important that the fundamental processes controlling the SRB in a given model are accurately simulated at the process level. Since the simulated SRB is mainly controlled by downwelling shortwave (SWD) and longwave (LWD) radiation, it is therefore highly dependent on the representation of cloud amounts, microphysical processes and cloud-radiation interaction. Due to their extreme complexity, cloud-radiation interactions are highly parameterized in present-day models. As mentioned in the IPCC 4th Assessment Report (Randall et al. (2007)), large differences exist between climate models in their simulated cloud radiation feedbacks, this being the main source of uncertainty in climate model sensitivity to a doubling of atmospheric CO_2 (Bony et Dufresne (2005), Soden et Held (2006)). In order to make reliable estimates of future climate conditions, it is therefore crucial that further improvements are made in our ability to simulate the fundamental physics controlling the SRB.

While climate models reproduce with some accuracy the seasonal mean SWD and LWD, this does not guarantee a correct representation of either the high-order SRB fluxes (e.g. the diurnal cycle) or the component physics controlling the total SRB (such as SWD and LWD for clear-sky or overcast conditions, or cloud amounts). A number of studies have evaluated simulated cloud amounts and SRB in climate models, often at the climatological scale and with different modeling tools, such as global climate models (GCMs), regional climate models (RCMs) or single-column models (SCMs).

GCMs are valuable tools to study cloud-radiation interactions as feedbacks (e.g surface radiation/ surface evaporation/ cloud formation) can develop in an internally consistent manner within the model (Cess et Coauthors (1996); Norris et Weaver (2001); Walsh

et al. (2002); Weare (2004); Stephens (2005); Martin et al. (2006); Williams et al. (2006)). This can help in improving the main feedback loops controlling the SRB. However, GCMs over a given region can suffer from circulation errors, often with an origin remote to the region of study that make it difficult to evaluate the simulated SRB against surface point observations.

At the opposite end of the modeling spectrum, SCMs use observed or analyzed thermodynamic and dynamical forcing to constrain a single vertical column of model parameterizations to follow the observed atmospheric evolution over a given location. In this manner, detailed point observations can be used to guide parameterization development (Curry et Coauthors (2000); Iacobellis et al. (2003); Lenderink et al. (2004); Yuan et al. (2006)). The main drawbacks in using SCMs for parameterization development is the lack of interaction between the SCM physical parameterizations and the resolved scale dynamics of the model, as well as difficulties in easily defining the SCM horizontal resolution.

RCMs offer a compromise between GCMs and SCMs. The simulated large-scale meteorology can be partially constrained to follow the observed evolution through application of analyzed lateral boundary conditions (LBCs), while still leaving freedom for local interaction between the model parameterizations and the resolved dynamics. As a result of the constraints resulting from the application of analyzed LBCs, simulated RCM processes can be compared to point observations in a common thermodynamic/dynamic phase space (Hogan et al. (2001); van Meijgaard et Crewell (2005)). RCMs have most commonly been applied over mid-latitude regions (Roads et al. (2003); Meinke (2006); Willén et al. (2005)), where they experience a relatively high degree of control by the applied LBCs (Lucas-Picher et al. (2008)).

To have confidence in simulated cloud-radiation interactions, it is important that models are evaluated over a wide range of simulated variables and over a wide range of climate conditions. Markovic et al. (2008) evaluated three RCMs over North America against NOAA SURFRAD observations and found all the models overestimated SWD

in summer due to an underestimate of cloud cover. They also show that cloud cover and cloud-free SWD biases often compensate to result in an accurate SWD for all-sky conditions. Morrison et Pinto (2006) suggested that some parameters in simpler microphysics schemes are based upon mid-latitude observations and are inadequate for simulating Arctic clouds. Wyser et al. (2008) and Tjernström et al. (2008) evaluated 8 RCMs over the Arctic against SHEBA observations and found that the simulated cloud cover annual cycle was poorly reproduced by most models and improvements in the parameterization of cloud amounts and mixed-phase cloud microphysics were required to improve the overall performance of RCMs and particularly the SRB over the Arctic.

The limited-area version of the GEM model (Global Environmental Multi-scale Model, Côté et al. (1998); Zadra et al. (2008), hereafter referred to as GEM-LAM) is presently being evaluated for use as a new operational RCM for regional climate-change projection over Canada. Analysis of the SRB and associated controls on the SRB are an important part of this evaluation. In this study we evaluate in detail the cloud and radiation processes simulated by GEM-LAM. We concentrate on two sites from the Atmospheric Radiation Measurement (ARM) Program, with high quality observations of cloud and radiation, but radically different climates, the Southern Great Plains (SGP) site in central USA and the North Slope of Alaska (NSA) site in Barrow, Alaska. The paper is organized as follows. In section 1.2, the model, observations and evaluated variables are described. Section 1.3 presents a comparison between model results and observations, beginning with a brief evaluation of the large-scale meteorology simulated by GEM-LAM at the two ARM sites (section 1.31.3.1). This is followed by an analysis of the surface radiation fluxes and cloud fraction (CF) in sections 1.31.3.2 and 1.31.3.3. SRB is then split into clear-sky and overcast conditions to analyze in more detail the individual components controlling the total SRB (sections 1.31.3.4 and 1.31.3.5). Section 1.4 contains a discussion of the main results and recommendations for future work.

1.2 Methodology

1.2.1 Model description and integration

GEM-LAM employs a two-time-level semi-Langragian, fully implicit advection scheme and a one-way lateral boundary nesting strategy following Davies (1976). Surface albedo and surface fluxes of heat, moisture and momentum are calculated over four surface subtypes (land, water, sea ice and land ice, Bélair et al. (2003b), Bélair et al. (2003a)). Subgrid scale turbulent fluxes are calculated using an implicit vertical diffusion scheme with prognostic turbulent kinetic energy (TKE) and a mixing length based on Bougeault et Lacarrère (1989) (Bélair et al. (1999)). GEM-LAM uses a prognostic total cloud water variable with a bulk-microphysics scheme for non-convective clouds. Separation of total cloud water into liquid and solid is based on the local air temperature ranging from all ice at -40 °C to all liquid at 0 °C (Rockel et al. (1991)). The liquid and solid effective radii ($r_{eff,liq}$ and $r_{eff,sol}$) range from 4 to 17 μm (liquid) and 20 to 50 μm (solid) parameterized as a fonction of the local cloud liquid or ice water content (Lohman et Roeckner (1996)). Fractional cloudiness is based on a relative humidity threshold, which varies in the vertical (Sundqvist (1988)). Individual cloud layers are assumed to overlap in the vertical using a maximum-random cloud overlap. The deep convection scheme is that of Kain and Fritsch (Kain et Fritsch (1990), Kain et Fritsch (1993)), whereas a Kuo Transient scheme is used for shallow convection (Kuo 1965; Bélair et al. (2005)). The radiation scheme is due to Li et Barker (2005) and employs a correlated k-distribution (CKD) method for gaseous transmission, with nine frequency intervals for longwave and four for shortwave radiation. While the longwave spectrum and the near-infrared portion of the shortwave spectrum are treated using the CKD method, the rest of the shortwave spectrum is dealt with in frequency space with UVC, UVB, UVA and photosynthetically active radiation separately considered. The scheme treats the following gases interactively, H_2O, CO_2, O_3, N_2O, CH_4, $CFC11$, $CFC12$, $CFC113$ and $CFC114$. The clear-sky radiative effect of background aerosols is included based on the climatology of Toon et Pollack (1976). This simple climatology specifies maximum

aerosol loading at the equator and a decrease towards the poles, with different values for continents and oceans.

The model was run with a horizontal resolution of 0.5° and 53 vertical levels, extending up to 10 hPa. The model time step was 1800 s. Two geographically separate integrations were made for the period 1998 to 2004/05 both employing observed sea surface temperatures (SSTs) and sea-ice, deribed from the AMIP dataset, as the lower boundary conditions and ERA-40/ECMWF analyses as lateral boundary conditions. The two integration domains (shown in figure 1.1) are each centered on one of the ARM observation sites. The choice of the two sites is due to the radically different climate regimes sampled at the sites. The SGP site is dominated by convection during the summer while during winter, mid-latitude synoptic weather systems are dominant. For the NSA site, while experiencing year-round cloudy conditions, multilayered liquid or mixed-phase clouds are dominant during the summer, whereas in winter, mixed-phase and low-level ice clouds dominate (Intrieri et al. (2002); Shupe et al. (2005); Curry et al. (1996)). In this paper we develop a methodology to fully utilize the cloud and radiation observations at these two sites in order to evaluate the cloud and radiation processes in GEM-LAM. We suggest this approach could be followed in a more general evaluation of cloud-radiation processes in a wider number of RCMs. Furthermore, the procedure could be extended to other ARM sites with similar observational availability but different climate regimes (e.g. the ARM Tropical Western Pacific site).

1.2.2 Evaluated variables

We evaluate model and observed SWD and LWD as a function of CF, i.e. for overcast and clear-sky conditions separately, to isolate different interactions between radiation and first, atmospheric aerosols and water vapor and second, cloud liquid water. Clear-sky conditions are determined when CF is less than 10 %, whereas overcast conditions are for a CF of 90 % or more. This categorization is done separately for model and observations and then the evaluation is done on a set of overcast or clear-sky cases as a climatological analysis across a large range of common conditions. 10 % and 90 %

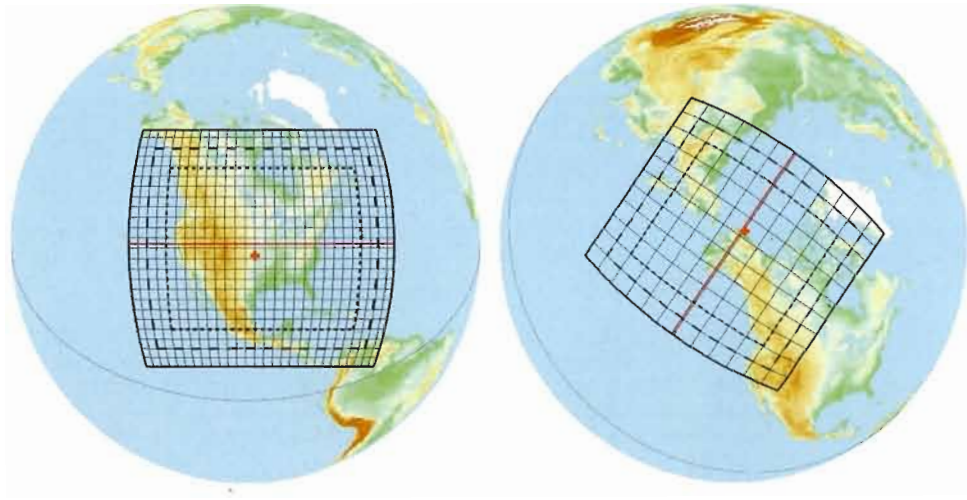

Figure 1.1 The two simulation domains centered over the ARM-SGP site (left) and the ARM-NSA site (right). Only every 5 grid points (left) or 10 grid points (right) of the original grids are shown while the dashed lines indicate nesting and sponge zones where the model is gradually forced to follow the LBCs. The observation sites are marked with a red cross.

are chosen as thresholds rather then 0 and 100 % in order to increase the dataset available for evaluation so that robust statistics can be achieved with respect to model performance.

Errors in simulated clear-sky conditions may arise from the different input to the radiation scheme (e. g. temperature, water vapor, aerosols and trace gases) or from the radiation scheme itself. In the presence of clouds, additional errors may arise from the simulated clouds (fraction, position, geometry), their water content as well as the assumed optical properties. In order to fully evaluate these individual components, we present an evaluation of the atmospheric water cycle, comparing the modeled and observed CF, liquid water path (LWP), integrated water vapor (IWV), precipitation and a preliminary evaluation of the aerosols optical depth (AOD). Ice water path (IWP)

would complete this evaluation but the available IWP observations seemed inconsistent at the time of our analysis. LWP and IWV are restricted to non-precipitating periods because of the unreliability of the microwave radiometer when the instrument is wet. Thus, modeled LWP and IWV are also filtered to exclude cases when precipitation is greater than 0.25 mm over a 3h period. The sensitivity of simulated LWP to the threshold defining precipitation removal is assessed in section 1.3.5.

We compare modeled variables at the grid point nearest to the relevant observation site. To reduce the representativity error between a single point observed variable and a modeled grid box mean variable, all variables are averaged or accumulated over three hour intervals (van Meijgaard et Crewell (2005); Hogan et al. (2001)). The period of comparison is from 1998 to 2004 for SGP and 1998 to 2005 for NSA.

The seasonal and diurnal cycles are the two largest forced modes of variability in the climate system, we therefore analyze the mean diurnal cycle of SWD, LWD and CF to identify systematic errors within the diurnal cycle that may contribute to seasonal mean errors. We also use three-hourly mean frequency distributions to compare modeled quantities such as LWP and precipitation to observations, in order to check that seasonal mean results do not result from higher time frequency error cancellation. Frequency distributions can also indicate under which meteorological/climate regimes the model differs most often from observations.

To complete our analysis, we plot three-hourly mean, co-variability plots of SWD and LWD versus LWP or IWV. This is done for overcast (LWP) and clear-sky (IWV) conditions separately for both model and observed quantities. This allows us to assess whether the model captures the underlying physical relationships of the cloud-radiation interaction controlling the simulated SRB.

1.2.3 Observation datasets

For the two sites, observations were obtained from the ARM Archive (http://www.arm.gov). Table 1.1 lists all the datasets used along with a quoted observational accuracy

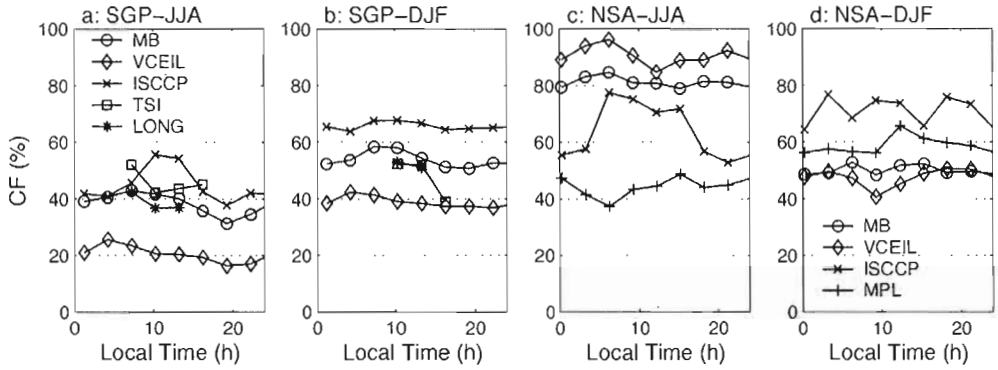

Figure 1.2 Mean diurnal cycle of different CF observations for (a) SGP summer and (b) winter for 2000-03, (c) NSA summer and (d) winter for 2004.

when reported. For the SGP site, all observations are extracted for the Central Facility (CF1) when available and if not, they were extracted from the extended facility E13. For the NSA site, all observations come from Barrow (C1).

For the two sites, CF observations are available from many different sources. We compared five different (different instruments or analysis) estimates for SGP and four estimates for NSA for a common period to evaluate their ability to detect the same CF and to determine a range of uncertainty in the CF observations. Figure 1.2 shows the mean diurnal cycle of three-hourly mean cloud observations, for summer and winter separately. The period for SGP is from June 2000 to December 2003, while for NSA, it covers only the year 2004. The five datasets for SGP are the CF derived from the shortwave radiation analysis of Long (stars) (Long et al. (1999)), the total sky imager (squares) (Kassianov et al. (2005)), the microbase cloud-radar dataset (circles) (Miller et al. (2005)), the ISCCP satellite data (crosses) (Rossow et Schiffer (1991), Rossow et Schiffer (1999)) and the Vaisala ceilometer (diamonds) (Lonnqvist (1995)). For the NSA site, the four datasets are from the Vaisala ceilometer (diamonds), the microbase cloud-radar dataset (circles), the ISCCP satellite data (crosses) and the micropulse lidar (plus signs) (Welton et Campbell (2002)).

Table 1.1 Datasets description for observations from the SGP and NSA sites.

Measurements	Data Identifier	Instruments	Accuracy/Limits
SWD, LWD & Albedo	beflux1long	pyranometer, pyrgeometer, pyrheliometer	5-10 W m^{-2}
	qcradbeflux1long	same as beflux1long	5-10 W m^{-2}
LWP & IWV	mwrret1liljclou	microwave radiometer, ceilometer	$\approx$ 18 g m^{-2} for LWP $\approx$ 0.7 kg m^{-2} for IWV
Precipitation	1smos	tipping bucket	0.254 mm
	mettwr4h	capacitive rain detector	30 %
CF	15swfanalsirs1long	same as SWD & LWD	10 %
	tsiskycover	total sky imager	solar elevation angle $\geq 10°$
	microbasepiavg	millimeter cloud radar, microwave radiometer, sounding profile, ceilometer, micropulse lidar	
	vceil25k	ceilometer	max detection height of 7.5 km
	isccp	satellite imaging radiometer	$\approx$ 10 %
	mpl	micropulse lidar	max detection height of 18 km
Aerosols	aerosolbe1turn	shadowband radiometer, Raman lidar	
	nimfraod1mich	radiometer	

Figure 1.2 shows that, for SGP, the Vaisala ceilometer generally underestimates CF compared to the other observations, while ISCCP tends to overestimate CF for DJF compared to the other observations. For the ceilometer, the summer underestimate is likely explained by the maximum detection height of 7.5 km, which leads to an under-detection of upper-troposphere optically thin clouds (Lonnqvist (1995)). For ISCCP, the winter differences may arise from the documented problems satellites have in distinguishing winter season low-level clouds, where discrimination between a low-level cloud and snow-covered surface is difficult in the visible wavelengths, while discrimination between cloud-top infrared emission and surface emission is complicated due to the frequent presence of a low-level thermal inversion (Key et Barry (1989); Schweiger et Key (1992)). The Long, total sky imager and microbase CF generally agree within 5-15 % at SGP for both seasons. For this reason, we used these three datasets in our analysis, averaging the three datasets every three hours when all three are available. If one or two datasets are not available at a given time, the datasets that are available are used as the observed CF. For the NSA site, the Vaisala ceilometer seems to match more closely the microbase dataset (clouds being generally located at a lower altitude at NSA compared to SGP means the 7.5 km height limit of the ceilometer is less of a problem), whereas the micropulse lidar seems to underestimate CF during the summer season compared to the other datasets. Based on the close agreement between the ceilometer and microbase datasets, we decided to average the three-hourly CF from these two datasets to provide the observed CF used in our analysis. The reader is reminded that the CF observations do not agree and to some extent this level of disagreement should be viewed as an observational uncertainty (of order $\pm$ 15 %) that varies with season. This level of accuracy should be borne in mind when specific cloud-radiation parameters are analyzed and indicates the critical importance attached to accurate cloud fraction observations.

1.3 Results

1.3.1 Large-scale meteorology

This section gives a brief overview of the model's ability to reproduce the large-scale meteorology at the two observation sites. We do this to confirm that the simulated atmosphere generally follows the observed evolution, allowing cloud-radiation processes to be evaluated against observations in a common thermodynamic phase space. We also make a preliminary analysis of the simulated 2 m temperatures at the two sites in order to later relate the impact of SRB errors on such a key variable.

As a measure of the large-scale synoptic variability, in figure 1.3 we plot the 3-day mean surface pressure and IWV for the model grid box collocated with each observation site and the same observed quantity. We choose one representative summer and winter season from the 7 to 8 years of analysis for each observation sites, other seasons being generally similar. For surface pressure, the synoptic variability is well reproduced by the model at NSA during the summer (JJA) and winter (DJF) seasons with only occasional small biases. For SGP, the variability is well reproduced by the model during the winter. Larger differences are seen at SGP during the summer season, as might be expected when the model atmosphere is less constrained by the LBCs (Lucas-Picher et al. (2008)). There is no apparent systematic surface pressure bias in any of the seasons or locations. Once the model is corrected for the altitude difference at SGP, the model reproduces well the observed amplitude of surface pressure for both sites and seasons. For IWV, the model, without any correction applied, reproduces the observed variability better in winter at both sites, also likely due to the stronger control by the LBCs in winter.

In figure 1.4 we present the observed and simulated mean diurnal cycle of 2 m temperature, for JJA and DJF seasons at both SGP and NSA sites. These are an average over 7 years for SGP and 8 years for NSA. At SGP, GEM-LAM has a warm bias of ≈ 5 °C through out the diurnal cycle for JJA although the actual amplitude of the diurnal cycle is well captured. At NSA, in the summer season, a nocturnal warm bias of ≈ 1 °C

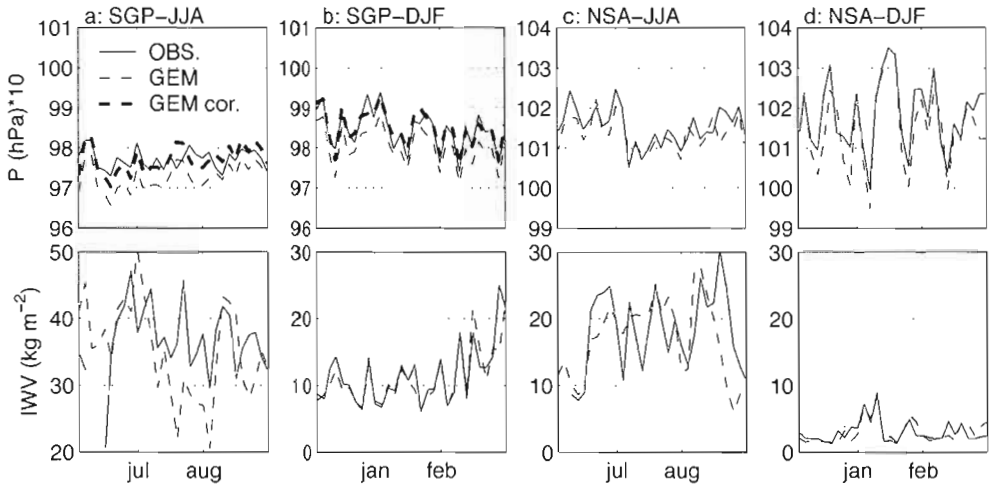

Figure 1.3 Three-day mean surface pressure (P) and IWV at SGP for (a) summer 2000, (b) winter 2000/01, and NSA for (c) summer 2004 and (d) winter 2004/05. For SGP, the thick dashed line represents a correction of 4.47 hPa applied to the modeled surface pressure to account for the 38 m difference in altitude between observations and model.

increases to 3 °C during the afternoon period. We will subsequently indicate that both of these errors are strongly correlated with excess SWD at the surface. During the winter season, the model reproduces quite accurately the diurnal evolution of 2 m temperature at both locations. The SGP-JJA temperature error is local to central North America and does not appear linked to major circulation errors. One possible cause of the warm bias might be an underestimate of surface albedo, which for an accurate SWD would lead to too much SWD being absorbed and warm the surface. Figure 1.5 shows a comparison of surface albedo at SGP and NSA between observed estimates (Shi et Long (2002)) and those used in GEM-LAM. In general, GEM-LAM has a realistic value of the surface albedo at both sites although there is a failure to represent the observed diurnal cycle of surface albedo, linked to the changing solar zenith angle. The deviations of albedo at SGP-JJA are certainly too small to explain the warm bias seen

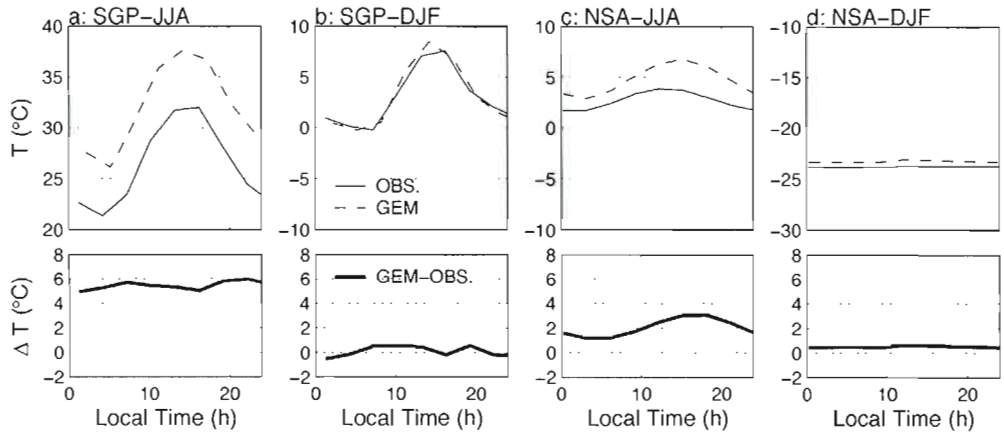

Figure 1.4 Mean diurnal cycle of three-hourly mean 2 m temperature for (a) SGP-JJA, (b) SGP-DJF, (c) NSA-JJA and (d) NSA-DJF. The bottom row shows corresponding bias.

in figure 1.4.

1.3.2 All-sky surface radiation fluxes

In this section we compare simulated and observed mean annual and mean diurnal cycles of SWD and LWD, for JJA and DJF respectively. This analysis is done for all-sky conditions. A more detailed analysis follows in sections 1.31.3.4 and 1.31.3.5, where CF is used to isolate the separate roles of water vapor or cloud liquid water on surface radiation. Figure 1.6 shows the mean annual cycle of SWD and LWD at both SGP and NSA. GEM-LAM overestimates SWD during the spring and summer by $\approx$ 15-20 W m^{-2} at SGP, while this overestimate is concentrated only in the summer season at NSA, but reaches $\approx$ 30 W m^{-2} with a smaller underestimate during spring. LWD is slightly overestimated during summer at SGP ($\approx$ 10 W m^{-2}) and underestimated by a similar magnitude in winter. At NSA, summer and fall LWD are underestimated by $\approx$ 10 W m^{-2}, while winter shows a positive LWD bias of similar magnitude. The quoted

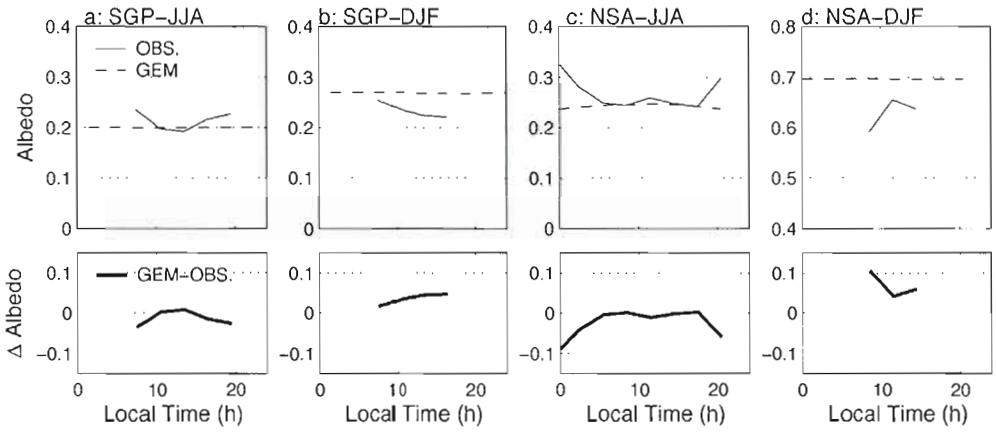

Figure 1.5 Mean diurnal cycle of three-hourly mean surface albedo for (a) SGP-JJA, (b) SGP-DJF, (c) NSA-JJA and (d) NSA-DJF. The bottom row shows corresponding bias.

observational accuracy of SWD and LWD are $\pm$ 10 W m^{-2} and $\pm$ 5 W m^{-2} respectively.

To better understand the source of errors in the SWD and LWD annual cycles, we begin by constructing mean diurnal cycles of SWD and LWD from both model and observations. Figure 1.7 shows the mean diurnal cycle of three-hourly mean SWD and LWD for summer (JJA) and winter (DJF) at both sites. The overestimate of seasonal mean SWD at both SGP and NSA is clearly associated with a developing SWD overestimate in the middle of the day with a $\approx$ 40 W m^{-2} maximum overestimate for SGP-JJA, $\approx$ 30 W m^{-2} for SGP-DJF and $\approx$ 50 W m^{-2} for NSA-JJA.

Positive and negative biases seen in the mean annual cycle for LWD are also visible through the diurnal cycle during JJA and DJF. For SGP-JJA, the overestimate is maximum ($\approx$ 15 W m^{-2}) in early afternoon and stays posiive for the rest of the day. The SWD overestimate seen at SGP-JJA likely causes the positive 2 m temperatures bias (reasons for this will be discussed in more detail in section 1.31.3.4) and this later bias is probably the direct cause of the LWD overestimate. The difference in

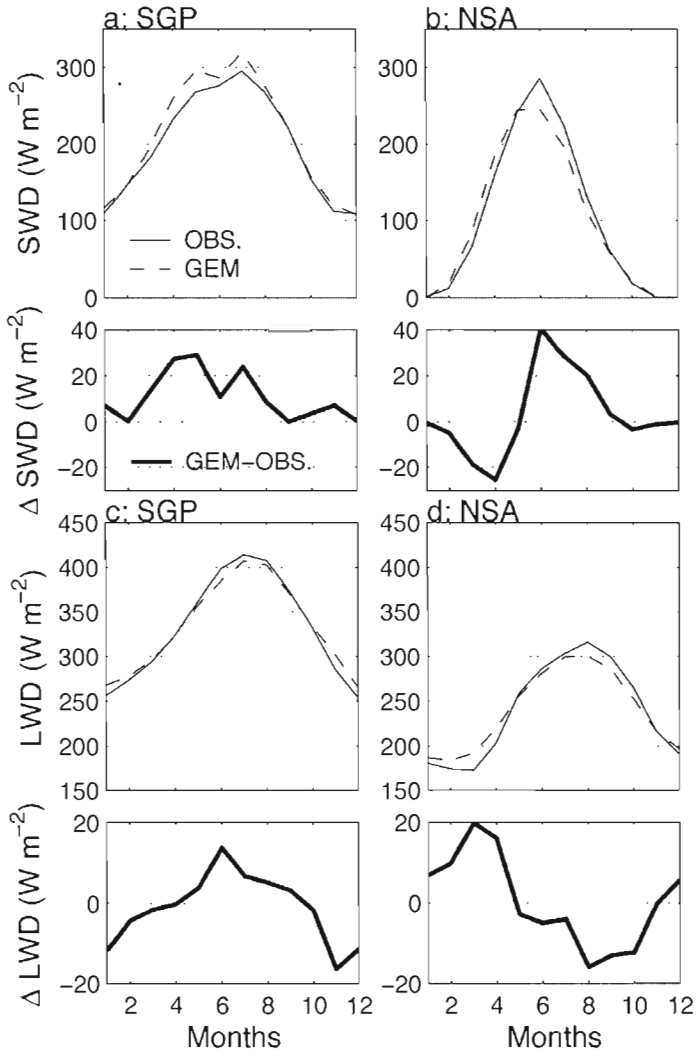

Figure 1.6 Mean annual cycle of monthly mean (a-b) SWD and (c-d) LWD at the surface for (a/c) SGP and (b/d) NSA with corresponding bias.

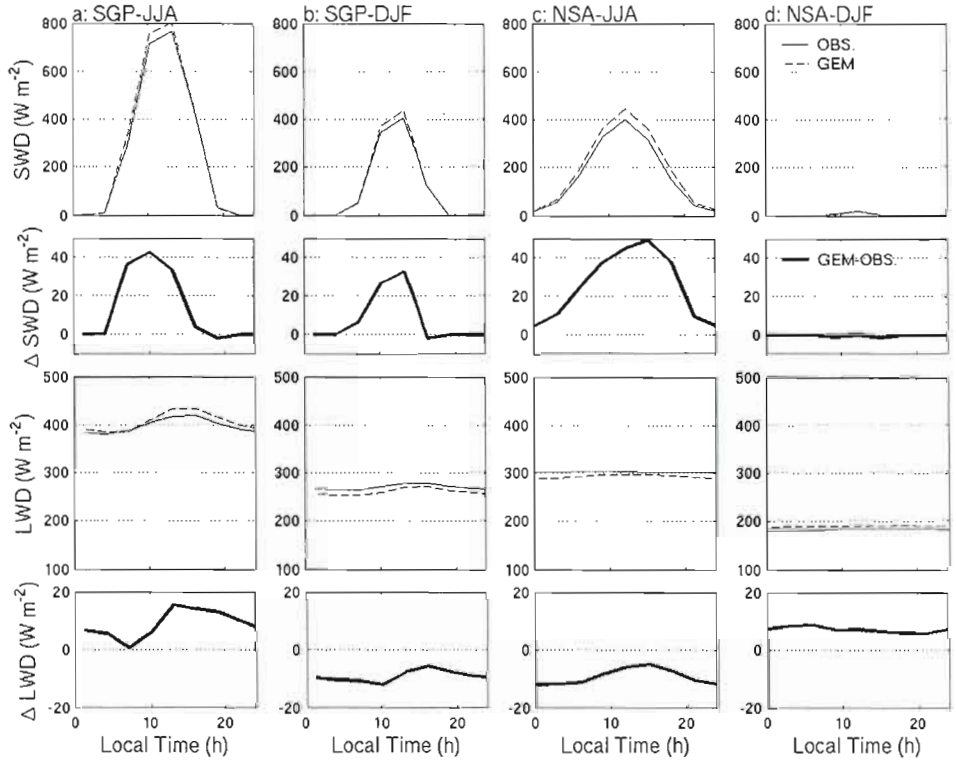

Figure 1.7 Mean diurnal cycle of SWD and LWD at the surface for (a) SGP-JJA, (b) SGP-DJF, (c) NSA-JJA and (d) NSA-DJF with corresponding bias.

near-surface temperature between model and observations at SGP during the summer season (a warm bias of ≈ 5 °C as shown in figure 1.4) would lead directly to a $\approx$ 20-30 W m^{-2} difference in LWD, assuming surface downwelling LWD emanates mainly from near-surface emission and applying a value of 0.73-0.85 for the near-surface atmospheric emissivity (Swinbank (1963), Chen et al. (1991)). This LWD overestimate, due to near-surface thermal errors, is partially balanced by a cloud underestimate at SGP-JJA (see figure 1.8 a) which acts to reduce the total sky emissivity in GEM-LAM compared to observations. For SGP-DJF and NSA-JJA, the LWD biases also show a diurnal cycle with a maximum underestimate of $\approx$ 12 W m^{-2} before local noon whereas for NSA-

DJF, the overestimate of 7 W m^{-2} is constant through the diurnal cycle but is within the observational uncertainty (Shi et Long (2002)).

1.3.3 Cloud fraction

Simulated cloud cover plays a key role in determining overall biases in SRB. In order to evaluate the full range of processes controlling the model SRB, it is necessary to first analyze the simulated and observed cloud fields. This is to both directly evaluate the impact of cloud errors on the total SRB, but also to allow for the separation of SRB errors into those directly associated with CF and those attributable to errors in either clear sky radiation (e.g. aerosols or water vapor impacts on radiation fluxes) or overcast radiation (e.g. representation of cloud reflection and/or cloud-radiation scattering/absorption). An analysis of all these three components, that each contribute to the all-sky SRB, will aid in identifying specific parameterization terms requiring improvement in GEM-LAM.

Figure 1.8 shows the mean diurnal cycle of three-hourly CF, separately for JJA and DJF, at SGP and NSA. The observed CF is an average of the estimates (Long/TSI/MB for SGP and Vceil/MB for NSA) shown in figure 1.2. We remind the reader that a degree of uncertainty exists regarding the absolute accuracy of the observed CF, of $\pm$ 15 %. GEM-LAM generally underestimates CF, ranging from $\approx$ 10 % at SGP for summer and winter, to $\approx$ 20 % at NSA in JJA. In the winter season GEM-LAM overestimates CF at NSA by $\approx$ 25 %. It is well established that most observational platforms have difficulty in detecting optically thin clouds that may be quite frequent at NSA in the winter. Wyser et Jones (2005) showed that by filtering modeled clouds to preclude all clouds with an optical thickness of less than 0.5, the resulting model CF was reduced by $\approx$ 20-25 % in the winter season over the Arctic. Futhermore, Karlsson et al. (2008) determined that the minimum cloud optical thickness detection limits for the Advanced Very High Resolution Radiometer (AVHRR) satellite are 1.0 and 3.0 for low-level clouds at night and twilight respectively. Therefore, the NSA winter cloud bias in GEM-LAM should be treated with some caution. Figure 1.9 shows a normalized frequency distribution

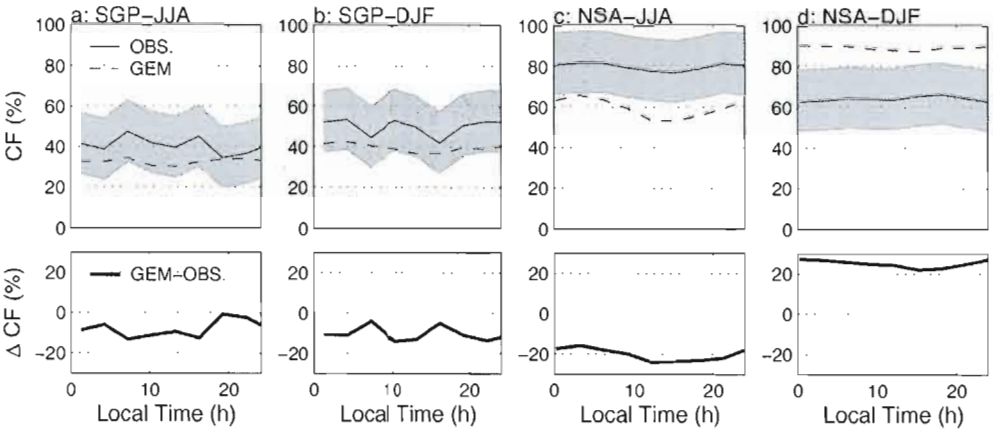

Figure 1.8 Mean diurnal cycle of CF for (a) SGP-JJA, (b) SGP-DJF, (c) NSA-JJA and (d) NSA-DJF. The light shaded zone around the observed curve represents a degree of uncertainty regarding the absolute accuracy of the plotted observed CF ($\pm$ 15 %). The bottom row shows corresponding bias.

of 3-hourly mean CF occurrences at SGP and NSA. While the general shape of the frequency distribution is well captured by GEM-LAM, the small underestimate in SGP clouds appear mainly due to an overestimate of clear-sky (CF $\leq$ 10 %) occurrences along with an underestimate of fractional cloud occurrences suggestive of an inability to simulate to simulate weakly forced convection in the summer over SGP. At NSA, the JJA underestimate in the mean CF is more a result of an underestimate of the occurrences of overcast conditions (CF $\geq$90 %).

The direct radiative effect of the CF underestimate at SGP in both seasons and at NSA in JJA, should be an underestimate of LWD and an overestimate of SWD. However, CF is not the only factor influencing the diurnal cycle of SWD and LWD. The clearest example of this can be seen for the overestimate of LWD during the summer season at SGP, even though CF is underestimated. To remove the direct influence of CF errors, in the following sections we analyze SWD and LWD separately for clear-sky and overcast conditions. With this method, we can better evaluate the physical processes controlling

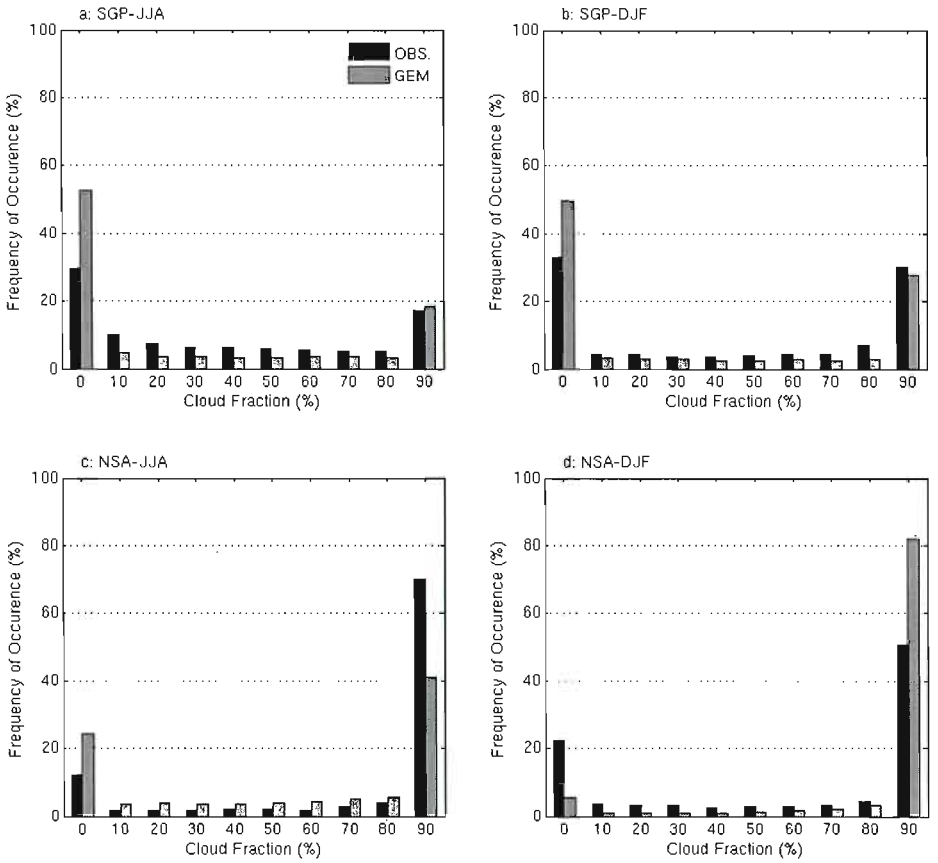

Figure 1.9 Frequency of occurrence of 3-hourly mean CF for (a) SGP-JJA, (b) SGP-DJF, (c) NSA-JJA and (d) NSA-DJF.

the overcast and clear-sky radiation fluxes in GEM-LAM and compare simulated relationships to those seen in the equivalent observations. Once we have a better idea of the model performance in these two regimes, in combination with the CF errors, we will be in a better position to attribute errors in the simulated SRB to the representation of specific processes in the model.

1.3.4 Surface radiation fluxes for clear-sky conditions

In this section we analyze surface radiation fluxes for clear-sky conditions only (CF $\leq$ 10 %). In this manner we can compare the representation of LWD and SWD fluxes isolated from the confounding effects of either CF or cloud-radiation parameterization errors.

Figure 1.10 shows the mean diurnal cycle of SWD and LWD for clear-sky conditions, this should be compared to figure 1.7 which shows the same quantities for all-sky conditions. The overestimate of total SWD for all-sky conditions is significantly reduced when only clear-sky conditions are considered. For SGP-JJA, the all-sky SWD overestimate of $\approx$ 40 W m^{-2} is reduced to below 20 W m^{-2} around local noon. Whereas, for SGP-DJF, the all-sky SWD overestimate now becomes an underestimate, of $\approx$ 20 W m^{-2} around local noon. Thus the simulated SWD in clear-sky conditions is not the main cause of the overestimate of all-sky SWD seen in figure 1.7, in fact the clear-sky errors tend to act in an opposite sense to the all-sky errors.

For LWD in clear-sky conditions at SGP, the same biases as LWD for all-sky conditions are seen, suggesting the LWD biases are largely controlled by near-surface temperature errors. For NSA-JJA, LWD in clear-sky conditions shows an overestimate of the diurnal cycle by the model resulting in a maximum overestimate of $\approx$ 15 W m^{-2} in the late afternoon. This clear-sky error is also likely tied to the near-surface warm bias at NSA-JJA which peaks in the late afternoon (figure 1.4) and appears directly caused by the excess all-sky SWD (figure 1.7). In terms of the all-sky LWD at NSA-JJA, the clear-sky overestimate in LWD is not seen because of the significant underestimate in

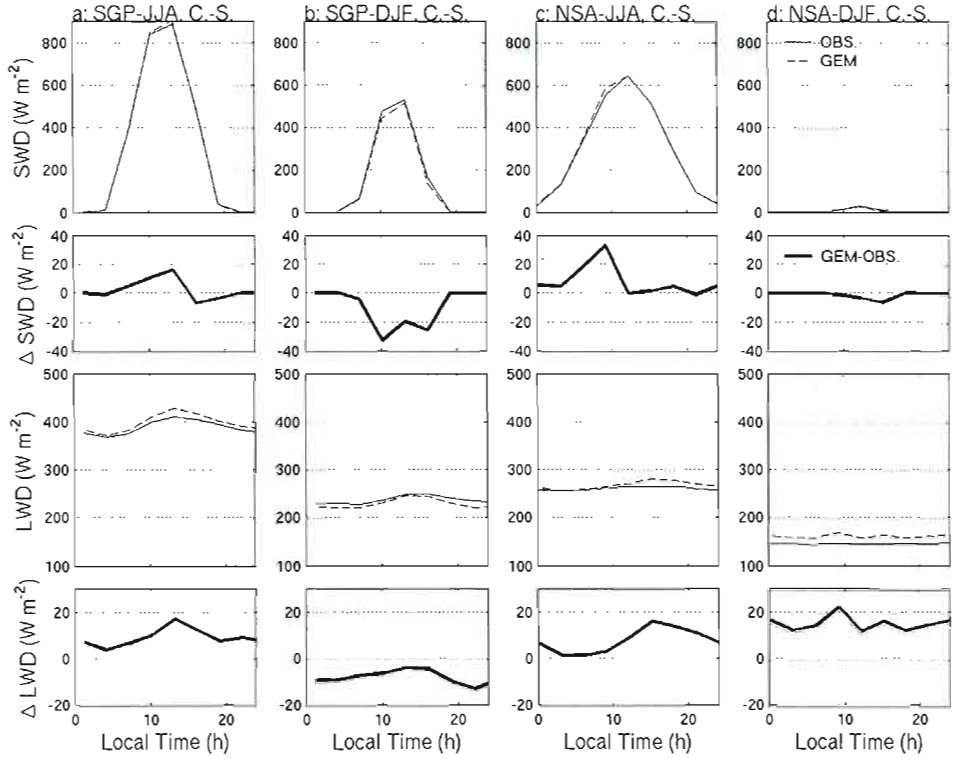

Figure 1.10 Mean diurnal cycle of SWD and LWD at the surface for clear-sky conditions for (a) SGP-JJA, (b) SGP-DJF, (c) NSA-JJA and (d) NSA-DJF with corresponding bias.

CF (peaking at $\approx$ 25 % in the afternoon), leading to an overall underestimate of all-sky emissivity, which completely offsets the thermal contribution to the clear-sky LWD. The final result being a negative bias in all-sky LWD at NSA-JJA. For NSA-DJF, the all-sky LWD positive bias of $\approx$ 7 W m^{-2} increases to $\approx$ 15 W m^{-2} in clear-sky conditions.

Atmospheric water vapor is one of the principal controls on the surface radiation budget in clear-sky conditions. Figure 1.11 presents the mean diurnal cycle of IWV. GEM-LAM underestimates the IWV throughout the diurnal cycle for SGP-JJA by $\approx$ 3.5 kg m^{-2} ($\approx$ 10 %). We will subsequently indicate that this bias may be correlated to an excess SWD

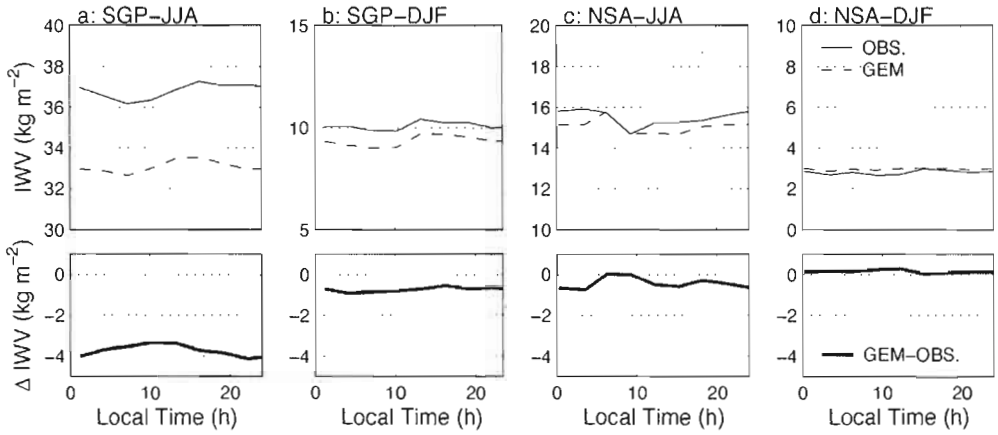

Figure 1.11 Mean diurnal cycle of IWV for (a) SGP-JJA, (b) SGP-DJF, (c) NSA-JJA and (d) NSA-DJF. The bottom row shows corresponding bias.

that may gradually lead to a surface dry bias. For SGP-DJF and NSA for both seasons, GEM-LAM reproduces the observed diurnal cycle of IWV quite accurately, within the quoted observational uncertainty of ≈ 0.7 kg m^{-2} (Turner et al. (2007)). These small underestimates of IWV may explain some of the SWD and LWD clear-sky errors in the model. The underestimate of IWV for SGP-JJA should lead to a clear-sky atmosphere with reduced emissivity and thereby an underestimate of LWD. Figure 1.10 shows that the warm bias in surface temperature for SGP-JJA outweighs the underestimate in IWV resulting in a positive bias in the clear-sky LWD.

To better understand errors in the simulated clear-sky SWD and LWD we present in figures 1.12 and 1.13 observed and simulated co-variability plots, between the three-hourly IWV and SWD/LWD for clear-sky conditions. Figure 1.12 shows the interaction between SWD and IWV. SWD is normalized by the solar zenith angle (SZA) with a maximum of 65°, to account for the geometrical increase in optical thickness as the SZA increases, commonly referred to as the air-mass factor (Wyser et al. (2008)). GEM-LAM reproduces the observed relationship for SGP-JJA and NSA-JJA within the limits of

available observations. At SGP-DJF the model exhibits a negative bias of $\approx$ 50 W m^{-2}. In other words, for a given amount of IWV, GEM-LAM simulates less SWD reaching the surface than observations suggest, as it is seen in figure 1.10. While we cannot fully identify the cause of this error, the accurate IWV-SWD relationship for the other sites and seasons, suggest the error likely lies outside of the direct IWV treatment. One probable cause is an excess aerosol loading over SGP in the winter, as the parameterization of Toon et Pollack (1976) gives a broadband aerosol optical depth (AOD) centered at 550 nm of 0.169 all year long whereas observations (Shi et Long (2002)) show a strong seasonal cycle of AOD at 500 nm from 0.063-0.095 for DJF to 0.170-0.199 for JJA. NSA-DJF is not shown because of a lack of SWD-IWV observations in clear-sky conditions. Offline radiation tests suggest halving the aerosol loading for typical mid-latitude winter conditions leads to a clear-sky SWD excess of 10 to 20 W m^{-2}.

Figure 1.13 depicts the interaction between LWD and IWV. At SGP in the summer season, GEM-LAM accurately represents the general relationship between increasing LWD and increasing IWV, although a constant positive bias of $\approx$ 25 W m^{-2} can be seen in the simulated clear-sky LWD irrespective of the IWV value. This error is a direct result of the warm near-surface temperature bias at SGP-JJA, as shown in figure 1.4 which we believe arises from the excess all-sky SWD in the summer season. Aside from this bias, it appears that the basic clear-sky LWD physics in GEM-LAM are accurately represented as the slope of the relationship between increasing IWV and increasing LWD is well captured by the model. For NSA-DJF, GEM-LAM also overestimates LWD reaching the surface (of $\approx$ 20-30 W m^{-2}) for a given amount of IWV but with little near-surface temperature errors. Again, the slope of the LWD-IWV relationship is fairly well captured by the model, suggesting the offset may arise from trace gas or aerosol contributions being overestimated. This bias leads to the overestimate in the clear-sky LWD diurnal cycle shown in figure 1.10.

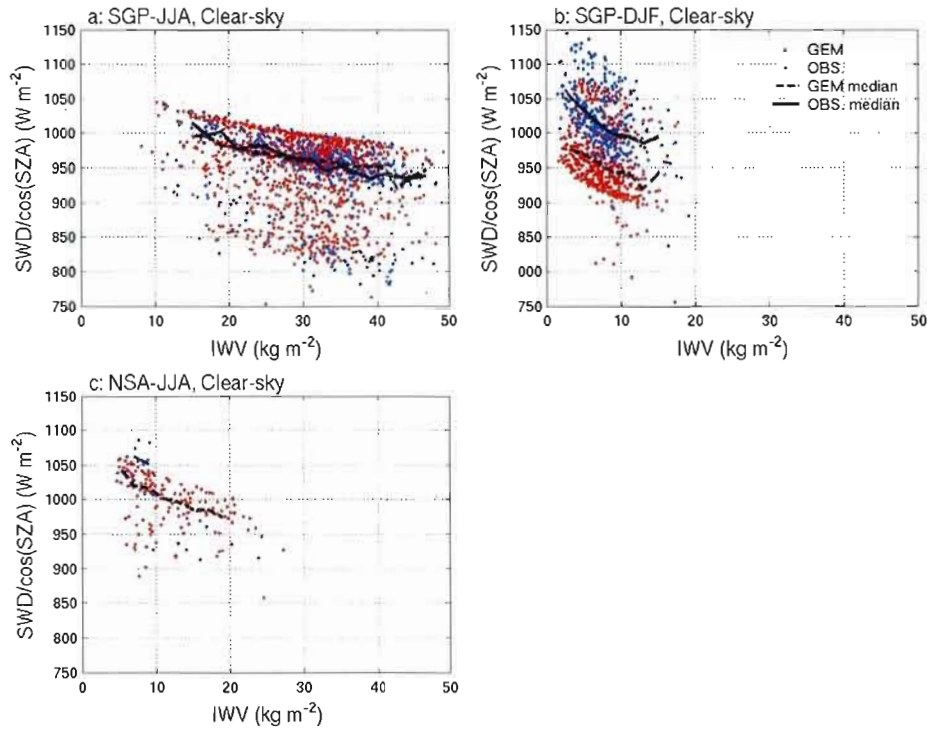

Figure 1.12 SWD as a function of IWV for clear-sky for (a) SGP-JJA, (b) SGP-DJF and (c) NSA-JJA. Median is plotted for model and observations. Shown are only values for SZA below 65°.

1.3.5 Surface radiation fluxes for overcast conditions

In this section, we present surface radiation fluxes for overcast conditions, i.e. when CF is $\geq$ 90 %. In doing this, we aim to isolate SRB errors arising solely from cloud microphysics and the overcast radiation parameterization, although clear-sky conditions above and below cloud cover do influence these findings somewhat. Figure 1.14 shows the mean diurnal cycle of SWD and LWD for overcast conditions. The overestimate seen in figure 1.7 for SWD (all-sky conditions) is now amplified for SGP-JJA (with a maximum overestimate of $\approx$ 150 W m^{-2} in the middle of the day). At SGP-DJF the

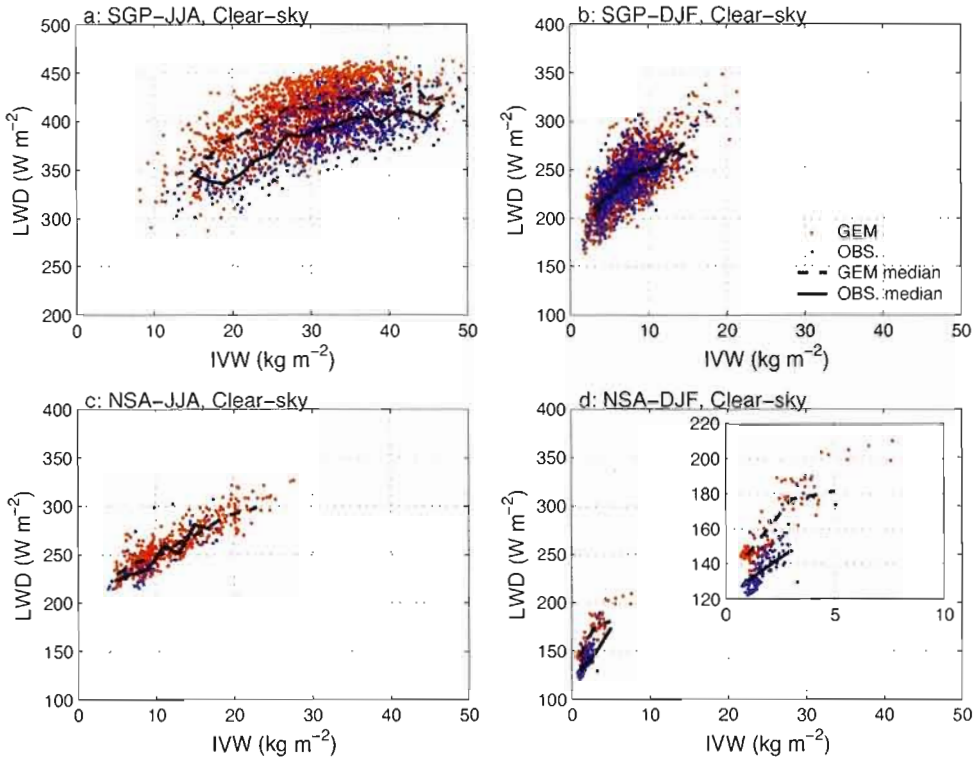

Figure 1.13 LWD as a function of IWV for clear-sky for (a) SGP-JJA, (b) SGP-DJF, (c) NSA-JJA and (d) NSA-DJF. Median is plotted for model and observations. The inset only represents a zoom over the results for NSA-DJF.

overcast SWD error is of similar magnitude and sign to the all-sky errors (≈ 30 W m^{-2}). At NSA-JJA, the all-sky SWD positive bias of ≈ 30 W m^{-2} (figure 1.7) in the afternoon becomes a negative bias of ≈ 70 W m^{-2} when only overcast conditions are considered.

For LWD in overcast conditions, GEM-LAM has a similar but less pronounced bias for SGP-JJA to that seen in figure 1.7 for all-sky conditions, again indicating the balancing effect of underestimated CF and overestimated near surface temperatures in relation to LWD. For all other seasons and sites, simulated LWD is close to the observational uncertainty, although it is noteworthy that small negative biases in LWD seen in figure

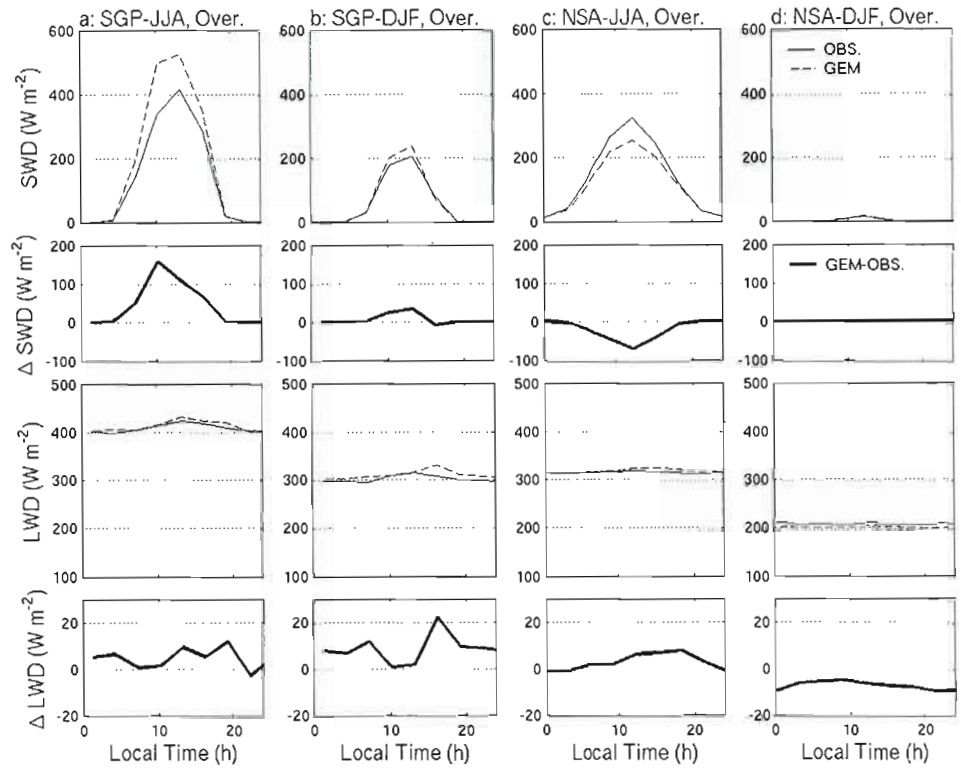

Figure 1.14 Mean diurnal cycle of SWD and LWD at the surface for overcast conditions for (a) SGP-JJA, (b) SGP-DJF, (c) NSA-JJA and (d) NSA-DJF with corresponding bias.

1.7 for SGP-DJF and NSA-JJA become small positive biases for overcast conditions and vice versa for NSA-DJF.

To better understand the SWD and LWD overcast errors, we directly evaluate the cloud liquid water amounts simulated by the model as well as analyzing the co-variability between SWD/LWD and cloud liquid water. Cloud water is the main factor controlling SWD and LWD for overcast conditions, influencing the radiation fluxes in a number of ways. The absolute quantity of cloud water controls both cloud albedo/absorptivity in the solar range and emissivity in the infrared range (Stephens et Webster (1981)), while

the partitioning into solid and liquid phase is also important, primarily for cloud-SWD interactions (Liou (1992)). Finally the actual droplet/crystal scattering and absorptivity/emissivity characteristics must be accurately represented, generally through a realistic estimate of both the droplet and ice crystal effective radii. The latter are highly parameterize in the model (see section 1.2.1) and are often very difficult to evaluate and constrain due to a lack of observations.

For the mean diurnal cycle of LWP for non-precipitating events, GEM-LAM underestimates LWP by $\approx$ 20 and 60 g m^{-2} for SGP-DJF and NSA-JJA respectively as seen in figure 1.15. The underestimate of LWP at SGP-DJF is consistent with the overcast SWD positive bias seen in figure 1.14. For NSA-JJA, the negative bias in LWP is definitely not consistent with the negative bias in overcast SWD. As cloud albedo is a non-linear function of LWP (Stephens and Webster 1981; Slingo 1989), it is not sufficient just to analyze the mean diurnal cycle of LWP, it is also necessary to establish how GEM-LAM simulates the range of variability of LWP at higher time frequency (i.e. the underlying LWP statistics that make up the mean values). In doing this, we may also better understand the physical processes in the model leading to the underestimate of LWP noted for SGP-DJF and NSA-JJA. To analyze LWP variability, we utilize a normalized frequency histogram approach as used previously by van Meijgaard et Crewell (2005). We bin all observed and simulated 3-hourly mean LWP and normalize each bin by dividing by the total number of LWP occurrences in either the entire observation or model dataset. This is done for non-precipitating events (defined as precipitation $\leq$ 0.25 mm $(3h)^{-1}$) and the histograms are made separately for JJA and DJF at both NSA and SGP sites. Results are presented in figure 1.16. One should be aware of the logarithmic profile of the y axis in figure 1.16 which influences the absolute size of LWP errors depending on whether they are at the lower or higher end of the distribution. The quoted accuracy for the LWP observations is $\approx$ 18 g m^{-2} derived from a 0.5 K radiometric uncertainty (Turner et al. (2007)), hence the first bin in our analysis encompassing the range 0 to 15 g m^{-2} is uncertain whether it represent clear-sky conditions or not.

For all cases, GEM-LAM overestimates the frequency of occurrence of LWP in the 0 to

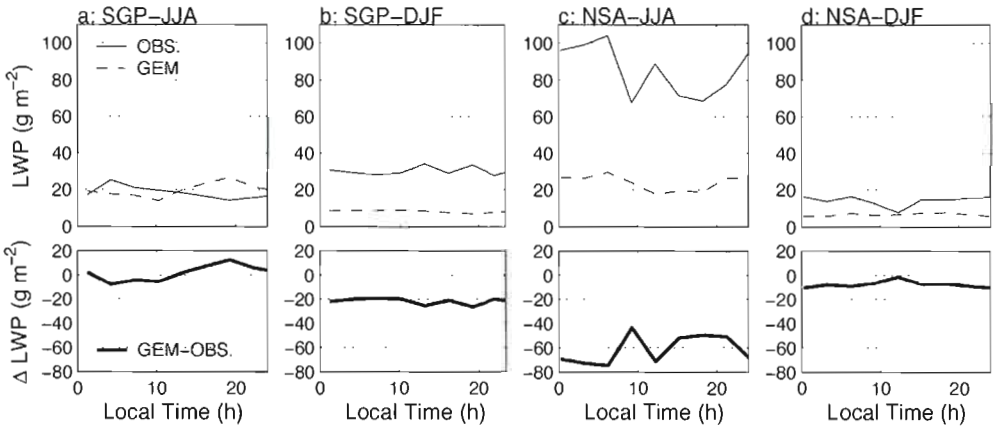

Figure 1.15 Mean diurnal cycle of LWP for (a) SGP-JJA, (b) SGP-DJF, (c) NSA-JJA and (d) NSA-DJF. The bottom row shows corresponding bias.

15 g m^{-2} range. This is particularly true for NSA-JJA. For SGP-JJA, GEM-LAM also overestimates the frequency of occurrences for LWP $\geq$ 165 g m^{-2}. In contrast, GEM-LAM underestimates the frequency of occurrence of higher LWP amounts for SGP-DJF ($\geq$ 45 g m^{-2}), leading to a reduced cloud albedo and excess SWD as seen in figure 1.14. At NSA, LWP ($\geq$ 15 g m^{-2}) is underestimated in both seasons, which should lead to an excess SWD in GEM-LAM under overcast conditions, this however is opposite to what is not seen in figure 1.14. The histogram statistics are consistent with the mean LWP diurnal cycle (figure 1.15) which presented negative biases in LWP for the SGP-DJF and NSA-JJA cases and a smaller negative bias for NSA-DJF.

One possible cause of an underestimate of LWP is that GEM-LAM reasonably simulates the total cloud water (ice and liquid) but has a poor fractional separation of the total water into the two respective phases. Unfortunately, we did not have access to reliable IWP observations to evaluate the simulated IWP in the model. Hence in figure 1.16, we present the simulated total condensed cloud water (CWP=LWP+IWP) (green line) for non-precipitating events. For SGP-DJF and NSA-JJA, inclusion of simulated IWP does not appear to greatly change the findings that LWP (and now CWP) is underestimated

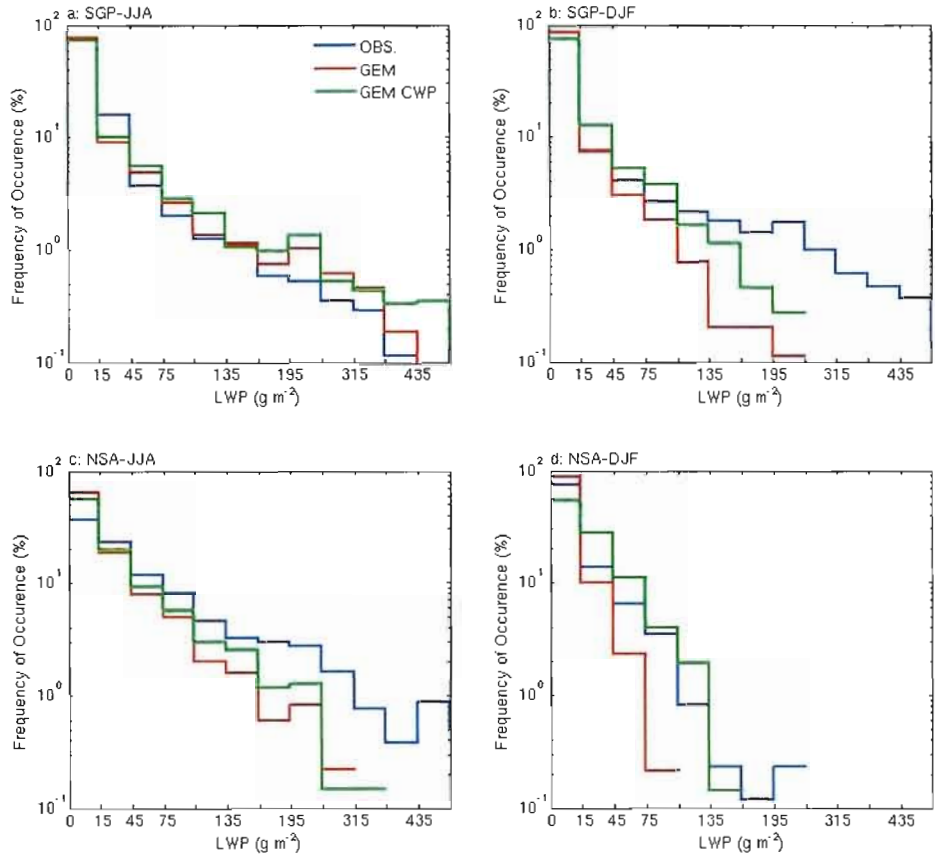

Figure 1.16 Frequency of occurrence of 3-hourly mean LWP and CWP (liquid+ice) for (a) SGP-JJA, (b) SGP-DJF, (c) NSA-JJA and (d) NSA-DJF.

in GEM-LAM for classes of LWP $\geq$ 45 g m^{-2} ($\geq$ 105 g m^{-2} for CWP at SGP-DJF). This does not preclude the possibility that IWP values are underestimated in GEM-LAM but it does suggest that the total cloud water in the model atmosphere is likely underestimated for SGP-DJF and NSA-JJA. In contrast, an incorrect separation of CWP in LWP and IWP may be the possible cause of the underestimate of LWP for NSA-DJF as the frequency of occurrence of simulated CWP includes and exceeds the occurrence frequency of observed LWP for the range between 15 and 135 g m^{-2}.

Another possible cause of an underestimate of LWP is that precipitation removal of cloud water occurs at too low LWP values in GEM-LAM microphysics scheme. Figure 1.17 presents simulated LWP filtered using different precipitation thresholds: the original threshold of 0.25 mm $(3h)^{-1}$ (red line) that is the same threshold used for the observations (blue line). The light blue line shows LWP occurrences when a threshold of 1 mm $(3h)^{-1}$ is used for filtering GEM-LAM results, while the pink line shows LWP values in GEM-LAM for all events, irrespective of rain occurrence. At both SGP-DJF and NSA-JJA, the inclusion of light precipitation events results in a distribution of LWP closer to observations, while the inclusion of LWP for all cases, including all precipitation events, is now very close to the observed distribution. Inclusion of LWP when the model is precipitating increases the relative occurrences of LWP $\geq$ 75 g m^{-2}. For NSA-DJF, the inclusion of LWP for all cases of precipitation has an important impact only for classes of LWP $\geq$ 135 g m^{-2}. These results suggest that GEM-LAM, particularly for SGP-DJF and NSA-JJA, produces precipitation at a too low threshold of liquid water content (and hence LWP). Precipitation is an efficient sink for cloud water and therefore is likely responsible for a too efficient removal of liquid water from the simulated clouds. This type of problem is shared by a number of other models (van Meijgaard et Crewell (2005)).

Figure 1.18 shows the three-hourly accumulated precipitation frequency distribution for model and observations. The overestimate of simulated precipitation in the range 0.5 and 4 mm $3h^{-1}$ for SGP-DJF and NSA-JJA, confirms the tendency for LWP to be too efficiently removed by precipitation and suggests the need to modify the autoconversion

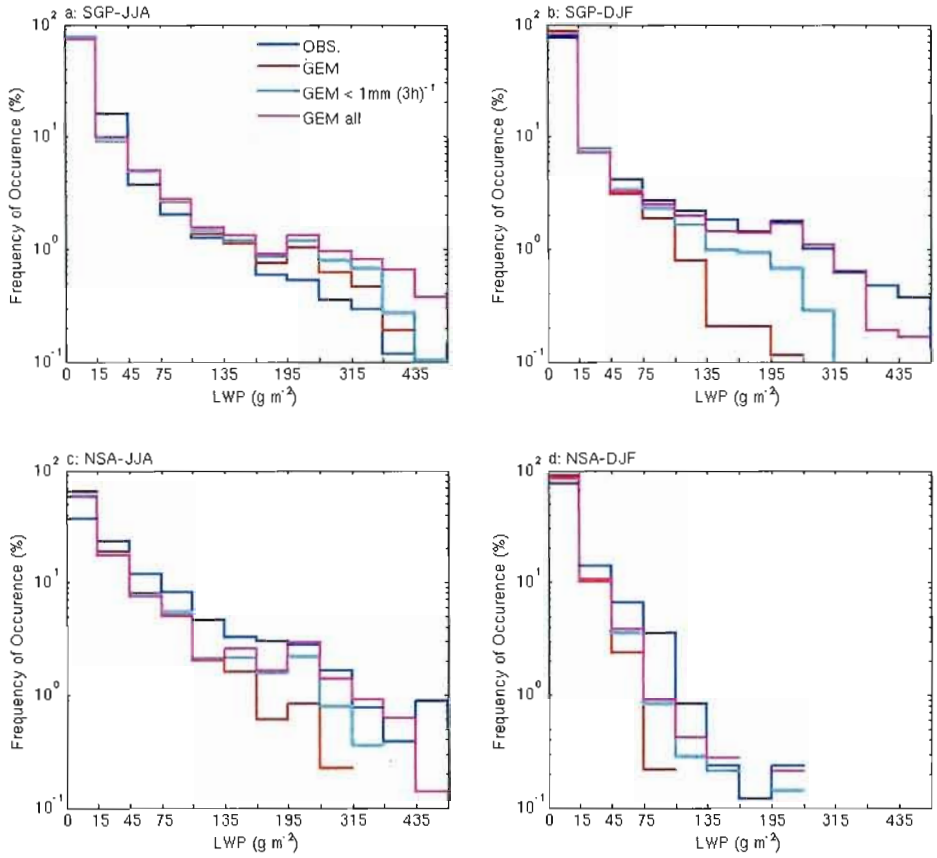

Figure 1.17 Frequency of occurence of 3-hourly mean LWP for different thresholds of precipitation for (a) SGP-JJA, (b) SGP-DJF, (c) NSA-JJA and (d) NSA-DJF.

term in the model microphysics.

The LWP analysis for SGP-JJA and NSA-JJA (accurate for SGP and an underestimate for NSA) show in figures 1.16 and 1.17 are not able to explain the overcast SWD errors seen in figure 1.14 (a positive bias at SGP-JJA and a negative bias at NSA-JJA), hence further analysis is required. In figures 1.19 and 1.21, we analyze the co-variability between LWP and either SWD or LWD. Three-hourly mean values of LWP are plotted against 3-hourly mean SWD or LWD fluxes for both model and observations. In figure 1.19, SWD is normalized by the solar zenith angle with a maximum angle of 85°.

Figure 1.19 shows that for a given LWP amount, the simulated SWD for SGP-JJA is systematically higher than observed, particularly for clouds with LWP values of less than 50 g m^{-2} with a maximum bias greater than 200 W m^{-2}. This positive bias in the relationship between SWD and LWP directly explains the positive bias seen in the overcast SWD diurnal cycle (fig. 1.14). Furthermore, GEM-LAM slightly overestimates the absolute LWP amounts during the afternoon at SGP-JJA (not shown) which will cancel out some of this positive bias for the afternoon period, resulting in a smaller overcast SWD bias, through error compensation. For SGP-DJF, a similar, albeit smaller positive bias in GEM-LAM SWD can also be seen compared to observations extending to clouds with larger LWP values. The cause of this bias is still unknown and is the subject of future research. At NSA-JJA, GEM-LAM better represents the observed co-variability between SWD and LWP, except for an underestimate of $\approx$ 50 W m^{-2} in the range 30 to 100 g m^{-2}. This result, combined with the LWP underestimate for NSA-JJA, cannot explain the entire overcast SWD underestimate seen in figure 1.14. NSA-DJF is not shown because of a lack of SWD-LWP observations in overcast conditions.

The SWD-LWP co-variability figures are done for non-precipitating events, due to the limitations of the microwave radiometer. In contrast, the SWD diurnal cycle for overcast conditions (fig. 1.14) is made for all occurrences of CF $\geq$ 90 %, irrespective of the precipitation occurrences. For consistency, we applied the same precipitation filter to

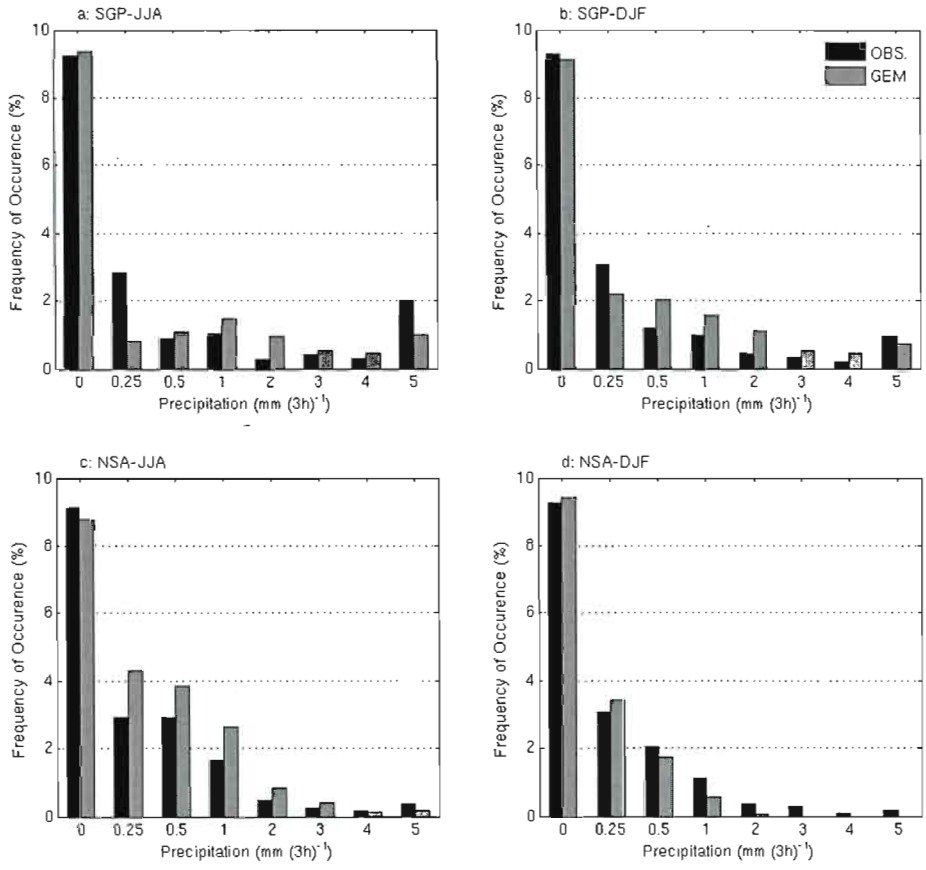

Figure 1.18 Frequency of occurence of 3-hourly accumulated precipitation for (a) SGP-JJA, (b) SGP-DJF, (c) NSA-JJA and (d) NSA-DJF. First bins from model and observations are divided by 10.

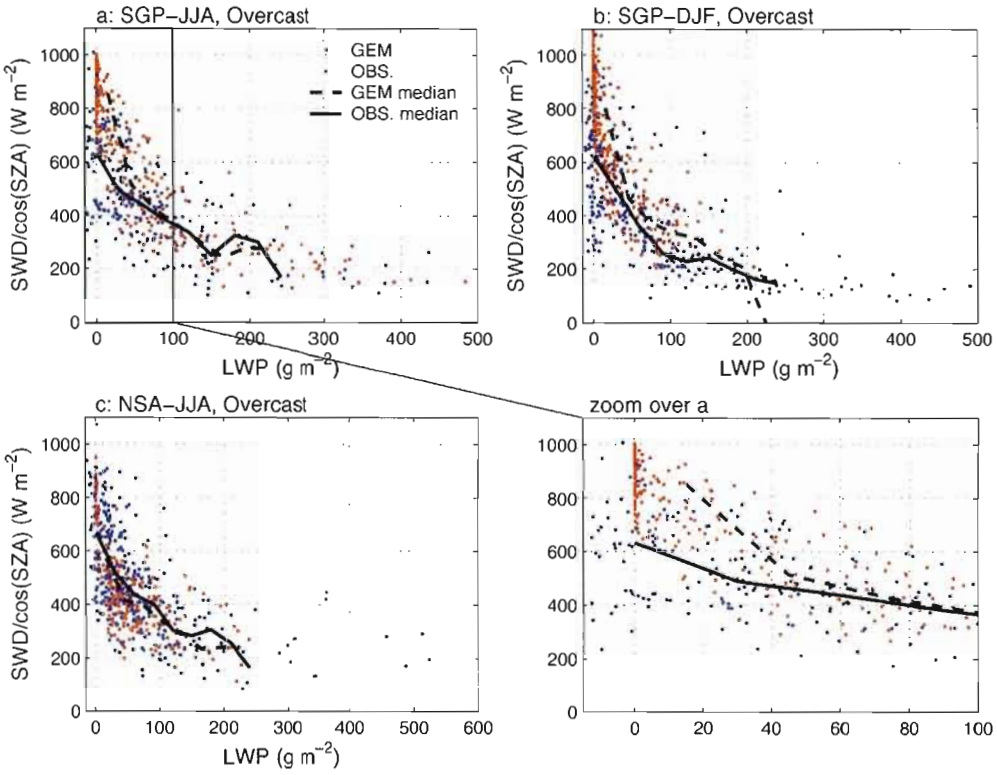

Figure 1.19 SWD as a function of LWP for overcast conditions for (a) SGP-JJA, (b) SGP-DJF and (c) NSA-JJA. Median is plotted for model and observations. The figure at the bottom right represents a zoom over the black box for SGP-JJA. Shown are only values for SZA below 85°.

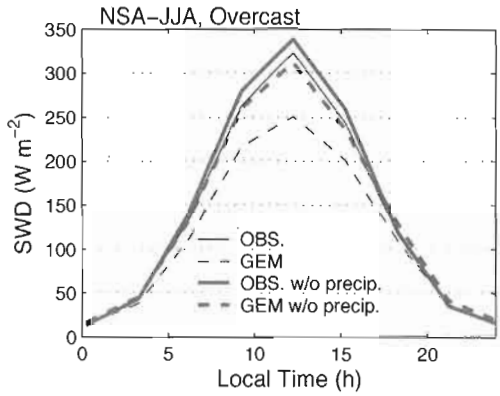

Figure 1.20 Mean diurnal cycle of SWD for NSA-JJA with and without precipitation.

the overcast SWD diurnal cycle for NSA-JJA. Figure 1.20 shows that when precipitating cases are removed for both model and observations (dashed lines), the underestimate in SWD for overcast conditions in GEM-LAM is reduced from $\approx$ 70 W m^{-2} to $\approx$ 25 W m^{-2}. This bias now agrees more closely with the SWD-LWP co-variability plot for NSA-JJA (figure 1.19) that shows an underestimate of SWD for clouds with LWP values of 30-100 g m^{-2}. A possible cause of this underestimate of solar transmissivity for optically thin clouds maybe that the effective radius calculation is tuned for mid-latitude conditions and requires an increased degree of flexibility to represent polar clouds where the dominant liquid and solid effective radii may be systematically larger than at mid-latitude regions. When precipitation is included in the overcast SWD mean diurnal cycle, the negative bias becomes larger, presumably due to the inclusion of more cloudy occurrences in the model compared to observations as the model overestimates the frequency of occurrence of precipitation (figure 1.18). Furthermore, these cases are skewed towards higher LWP amounts in the model than observations (figure 1.17, the pink line), contributing to the larger underestimate of overcast SWD.

Figure 1.21 shows that GEM-LAM accurately reproduces the rapid increase to saturated emissivity as a function of LWP at SGP during both seasons. The constant positive bias of $\approx$ 20 W m^{-2} seen for LWD in SGP-JJA for all ranges of LWP, again arises from the

warm near-surface temperature bias, which influences overcast LWD through clear-sky emission below cloud. For NSA-JJA, GEM-LAM also captures the rapid increase in emissivity in the lower range of LWP and the succeeding saturation. For NSA-DJF, the increase of LWD for low LWP is more visible and GEM-LAM tends to overestimate this by $\approx$ 30 W m^{-2}. This overestimate in LWD may also just be a reflection of errors in clear-sky emission below cloud base, as a similar bias was seen in figure 1.13 for NSA-DJF. Recent observations (Shupe et al. (2006)) suggest the liquid fraction in mixed-phase Arctic clouds tends to approach zero at temperatures of -25 °C to -30 °C. If this is the case, then the GEM-LAM parameterization to split total water into liquid and ice fractions will overestimate the liquid fraction at cold temperature. All other things being equal, this would contribute to an overestimate of LWD from winter clouds at NSA, as seen in the figure.

The general underestimate of LWP, seen in figure 1.16, has little impact on LWD for SGP (both JJA and DJF) and NSA-JJA in overcast conditions because the simulated clouds, even with a negative bias in LWP, remain at an emissivity of unity. LWP errors do have a larger impact for NSA-DJF, where the amount of LWP is very small and an underestimate of LWP will lead to a negative bias in cloud emissivity. One should bear in mind that clouds at NSA-DJF likely contain a significant amount of ice water and due to observation problems we are unable to gauge the contribution of IWP errors to LWD which are likely largest for NSA-DJF.

1.4 Conclusions and Discussion

In this paper, we have evaluated cloud-radiation interaction in the limited-area version of GEM, concentrating on the total surface radiation fluxes, as well as evaluating the various process level terms that contribute to errors in the total surface radiation flux. This has been done using observational data from two ARM sites (SGP and NSA) with radically different climates. The large-scale meteorology (defined here by three-day mean surface pressure and IWV variability) is accurately simulated at both sites, allowing a comparison of simulated cloud-radiation to point observations in a common

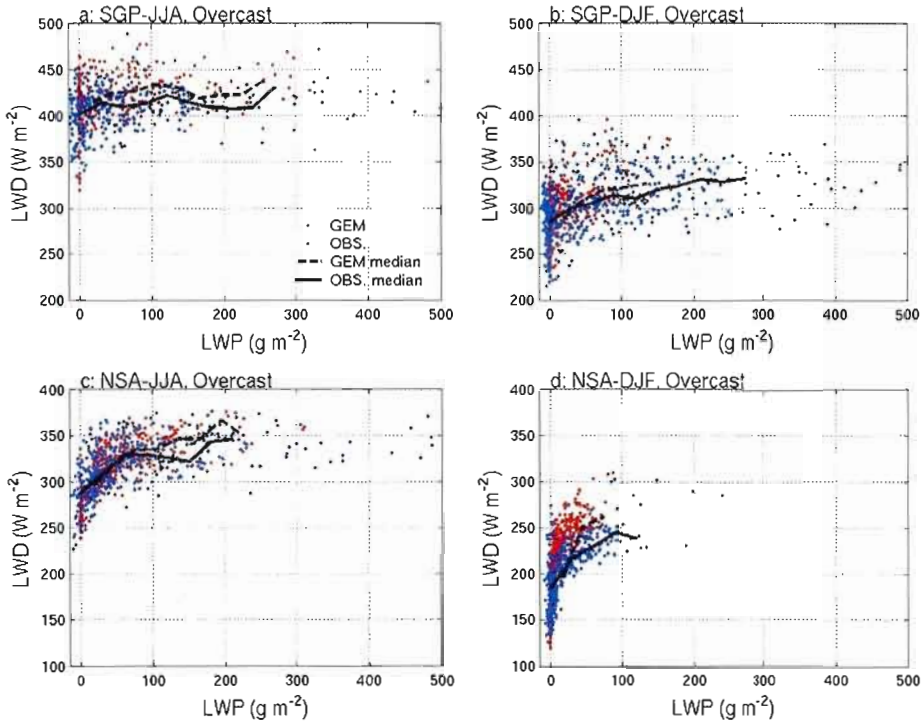

Figure 1.21 LWD as a function of LWP for overcast conditions for (a) SGP-JJA, (b) SGP-DJF, (c) NSA-JJA and (d) NSA-DJF. Median is plotted for model and observations.

thermodynamic/dymanic parameter range.

Comparison of the mean annual cycle and mean diurnal cycle of SWD showed that GEM-LAM generally overestimates SWD at all sites. GEM-LAM overestimates LWD at SGP in the summer while it underestimates LWD in the winter. For NSA, the model has relatively small LWD biases that lie within the range of observational uncertainty. Different processes contribute to these biases, CF errors influence the all-sky radiation, while aerosols and IWV are the primary terms controlling clear-sky solar radiation and both IWV and near-surface temperatures influence the clear-sky LWD. In overcast

conditions LWP amounts and their interaction with radiation is the primary variable.

GEM-LAM generally underestimates CF except at NSA for the winter where it appears to have a positive bias, although the latter error should be treated with caution due to known observational limits with respect to winter arctic clouds. The underestimate in CF is a strong contributing factor to the overestimate of all-sky SWD and underestimate in LWD. Nevertheless, we have shown that errors in clear-sky and overcast radiation fluxes also influence the all-sky radiation and sometimes lead to error cancellation. A clear example of this is the overestimate of SWD for NSA-JJA which results from an underestimate of simulated CF, a correct simulated clear-sky SWD and an underestimate of simulated overcast SWD (i.e. when clouds are present they are too reflective) which partially balances the CF underestimate.

The general underestimate of LWP in GEM-LAM only influences SWD in overcast conditions for SGP-DJF and LWD in overcast conditions for NSA-DJF. An overestimate of the occurrence of light precipitation in GEM-LAM appears to be the main cause of the negative bias in LWP at SGP-DJF and NSA-JJA, pointing to a need to improve microphysical conversion processes in the model.

GEM-LAM represented the co-variability between IWV and LWD in clear-sky conditions quite accurately, with a positive bias in LWD linked to a near-surface warm bias at SGP-JJA and NSA-JJA. At NSA-DJF, there is no clear thermal explanation for the clear-sky LWD bias, suggesting instead a possible erroneous contribution from aerosols or trace gases. For overcast conditions, the positive bias in LWD as a function of LWP for NSA-DJF is also likely a reflection of the aforementioned clear-sky bias. With respect to the co-variability of SWD-LWP, a positive SWD biases at SGP, for optically thin clouds, may be related to an incorrect separation of LWP and IWP and/or to a incorrect treatment of effective radii. Furthermore, since GEM-LAM uses a plane-parallel radiative transfert scheme, a more sophisticated 3D treatment of clouds could improve SWD bias at SGP. Tests on the parameterization of these variables are needed to improve the co-variability of SWD as a function of LWP. Furthermore, an opposite

bias in the SWD-LWP relationship was seen for optically thin clouds at NSA (surface SWD values being too small in the model for a given LWP value, when LWP < 30 g m^{-2}), suggesting a more flexible approach to the parameterization of cloud effective radii is required, that can more faithfully capture the differing underlying controls on cloud droplet/crystal size at various geographic locations (e.g. background aerosols loadings). Similar conclusions were made by Wyser et al. (2008) in their analysis of 8 RCM-simulated cloud-radiation interactions over the Arctic SHEBA site.

In summary the primary SRB error in GEM-LAM is the excess solar radiation reaching the surface in the middle of the day. This problem is common to SGP in both seasons and NSA in the summer. At SGP, this all-sky error is partly caused by an underestimate of cloud amounts, which is further compounded by an overestimate of SWD in the middle of the day during overcast conditions. The latter error is linked to an overestimate of solar transmissivity in optically thin clouds (LWP < 50 g m^{-2}) at SGP during both seasons. The absolute cause of this error remains to be determined. In contrast, at NSA-JJA the impact of a CF underestimate is partially offset in terms of the all-sky SWD by cloud solar transmissivity being too low (i.e. too little SWD reaching the surface in overcast conditions). This error is partly explained by an underestimate of solar transmissivity in optically thin clouds (LWP < 30 g m^{-2}) and is amplified in comparison to observations of overcast radiation by the inclusion of precipitating events as the model overestimates the frequency of occurrence of precipitation.

Excess SWD during the afternoon leads to the development of a warm near-surface temperature bias, particularly during the summer seasons at both SGP and NSA. This warm bias is the primary cause of excess clear-sky LWD at both sites in the summer. The excess clear-sky LWD is partially balanced with respect to the all-sky LWD by an underestimated CF, which even leads to a negative bias in simulated all-sky emissivity at NSA-JJA. An underestimate of LWP does not contribute significantly to errors in the overcast LWD at SGP or NSA during the summer due to the simulated clouds still having an emissivity of unity even with a negative LWP bias. Finally, the excess SWD may gradually lead to a surface dry bias, through excess evaporation and thus con-

tribute to the negative bias seen in IWV, particularly at SGP in the summer. Clearly, there is strong interaction between all the components influencing the simulated SRB with frequent error compensation. Nevertheless, the primary requirements for an improved SRB in GEM-LAM do appear to be a better estimate of the diurnal cycle of cloud amounts, likely requiring modification to the GEM-LAM convection and cloud fraction parameterization, and the description of the interaction of these clouds with solar radiation.

Acknowledgments.

Data were obtained from the Atmospheric Radiation Measurement (ARM) Program sponsored by the U.S. Department of Energy, Office of Science, Office of Biological and Environmental Research, Environmental Sciences Division. This study was supported by funding from the Mathematics of Information Technology and Complex Systems (MITACS, grant number 61851).

CONCLUSION

Cette étude a permis l'évaluation de l'interaction nuage-rayonnement du modèle GEM-LAM composantes par composantes afin d'identifier les différentes sources d'erreurs qui contribuent aux biais du rayonnement à la surface.

Ainsi, l'influence de la vapeur d'eau, de l'eau liquide des nuages ainsi que la fraction nuageuse sur le rayonnement de longues et courtes longueurs d'ondes a été évaluée en tentant de séparer les différentes contributions. Ces différentes variables du modèle ont été évaluées en les comparant aux observations de deux sites en Amérique du Nord ayant des conditions climatiques radicalement différentes, pour les saisons d'été et d'hiver. Les cycles diurnes saisonniers ont permis de comparer l'évolution des biais du modèle à une fréquence plus élevée que les moyennes mensuelles généralement utilisée. De la même façon, avec des statistiques moyennées sur trois heures, les distributions de fréquences ont permis d'idientifier certains biais dans l'eau liquide des nuages simulés par le modèle. Les relations de co-variabilité entre le rayonnement et la vapeur d'eau ou l'eau liquide ont permis d'évaluer la capacité du schéma de transfert radiatif et du schéma microphysique à représenter l'interaction nuage-rayonnement observée pour les différentes conditions climatiques.

Comme première étape, deux variables ont été évaluées sur des moyennes de trois jours, soit la pression de surface et la vapeur d'eau intégrée à la verticale, afin de vérifier l'hypothèse selon laquelle le modèle régional peut être assez bien contraint par ses conditions aux frontières latérales pour suivre l'évolution des grandes échelles observées. Le modèle réussisant à bien reproduire la variabilité synoptique des observations, ceci nous a permis de comparer les statistiques aux deux sites d'observations avec le modèle dans un espace semblable de paramètres dynamiques et thermodynamiques.

Ensuite, la première partie de l'analyse portant sur les cycles diurnes a montré une surestimation du rayonnement d'ondes courtes simulé (flux vers le bas, à la surface) par rapport aux observations pour les deux saisons au site SGP et pour l'été au site NSA. Ce biais positif est dû à une sous-estimation de la fraction nuageuse et, pour le site SGP, à une surestimation du rayonnement d'ondes courtes lors de conditions de ciel couvert (lorsque la fraction nuageuse $\geq$ 90 %). Ce dernier biais positif en ciel couvert est lié à une surestimation de la transmissivité des nuages optiquement minces pour le site SGP durant les deux saisons étudiées. Par contre, pour le site NSA en été, un biais inverse est noté, c'est-à-dire que le modèle sous-estime la transmissivité des nuages et ceci compense partiellement la sous-estimation de la fraction nuageuse qui est plus importante pour ce site en été, résultant en un biais semblable aux biais du site SGP pour le rayonnement d'ondes courtes pour toutes les conditions (indépendamment de la fraction nuageuse).

Le biais positif du rayonnement d'ondes courtes induit un biais positif de la température près de la surface, particulièrement pour la saison d'été aux deux sites. Ce biais est la cause principale de la surestimation du rayonnement de longues longueurs d'ondes dans les conditions de ciel clair (lorsque la fraction nuageuse $\leq$ 10 %) toujours pour la saison d'été aux deux sites. Ce biais positif des longues longueurs d'ondes est compensé par la sous-estimation de la fraction nuageuse, ce qui mène à des biais réduits ou à des biais opposés pour le rayonnement d'ondes longues pour toutes les conditions. Finalement, le biais positif de courtes longueurs d'ondes peut potentiellement mener à l'assèchement de la surface, par un excès d'évaporation et il peut ainsi contribuer au biais négatif de vapeur d'eau, particulièrement pour l'été au site SGP.

Ainsi, il est clair qu'il existe de fortes interactions entre les différentes composantes qui contrôlent le bilan radiatif de surface et que les erreurs compensatoires sont très fréquentes. Il est donc important d'analyser séparément ces composantes lors de l'évaluation de modèles climatiques.

En deuxième partie de l'analyse, les graphiques de co-variabilité ont permis de mettre en évidence certaines faiblesse des paramétrages des schémas microphysique et radiatif. Par exemple, le biais négatif noté seulement pour l'hiver à SGP dans la co-variabilité des courtes longueurs d'ondes et de la vapeur d'eau suggère que l'erreur ne provient pas du traitement direct de la vapeur d'eau par le schéma de transfert radiatif. La cause la plus probable est une surestimation des aérosols pour la saison d'hiver à ce site. Ces aérosols sont basés sur la climatologie de Toon et Pollack (1976) qui n'inclut pas de variabilité inter-annuelle contrairement à ce que les observations démontrent. Quant à la co-variabilité entre les longues longueurs d'ondes et la vapeur d'eau, malgré le biais positif du modèle pour l'hiver à NSA, la pente de la relation est bien simulée par le modèle. De plus, contrairement aux deux saisons d'été, aucun biais dans la température près de la surface ne peut expliquer ce biais. Ceci laisse croire que ce biais serait relié à la représentation des aérosols ou des gaz rares. Pour ce qui est de la co-variabilité entre le rayonnement d'ondes courtes et l'eau liquide des nuages, le modèle a un biais positif pour les nuages optiquement minces (LWP $\leq$ 100 g m^{-2}) pour le site SGP. Par contre, un léger biais opposé, soit négatif, est présent pour le site NSA pour les valeurs de LWP $\leq$ 30 g m^{-2}. Pour le site SGP, ce biais pourrait provenir d'une séparation erronnée entre l'eau liquide et l'eau solide du nuage ou encore d'un mauvais traitement des rayons effectifs de ces deux phases. Le biais opposé observé au site NSA suggère que la paramétrisation des rayons effectifs doit être plus flexible pour tenir compte des processus sous-jacents qui contrôlent la taille des hydrométérores et qui varient considérablement selon la situation géographique (par exemple, les concentrations d'aérosols). Ainsi, les aérosols prescrits dans le modèle sont une quantité à vérifier, tant du point de vue de leur distribution géographique et temporelle que de la paramétrisation de leurs interactions avec le rayonnement et de leurs influences sur les processus microphysiques.

Comme dernier volet de l'analyse, les résultats des histogrammes de l'eau liquide des nuages ont indiqué qu'une conversion trop rapide de l'eau des nuages en précipitation est responsable du biais négatif dans le modèle pour le site SGP en hiver et le site NSA en été alors que pour l'hiver à NSA, la séparation entre la phase solide et liquide de l'eau du

nuage dans le modèle semble être un facteur plus déterminant dans la sous-estimation de l'eau liquide simulée. Pour corriger ces biais, le terme d'autoconversion du schéma microphysique devrait être révisé afin que la production de précipitation soit retardée. Par ailleurs, différents schémas microphysiques à plusieurs moments et incluant plus d'une variables pronostiques pour représenter les différents hydrométéores sont maintenant disponibles pour être utilisés dans les modèles climatiques (Kong et Yau (1997) ; Milbrandt et Yau (2005a) ; Milbrandt et Yau (2005b) ; Morrison et al. (2005a) ; Morrison et al. (2005b)). Ces schémas tentent de représenter plus fidèlement les processus physiques présents dans les nuages et certains incluent l'effet des aérosols sur la formation de gouttelettes et de cristaux de glace à l'intérieur des nuages. Cependant, ce ne sont pas nécessairement les mêmes paramètres d'aérosols qui sont pris en compte par le schéma de transfert radiatif. Ainsi, pour améliorer le réalisme physique des processus sous-maille des modèles, un effort d'homogénéisation entre les différents schémas doit être fait. Le schéma de Milbrandt et Yau (2005a) à simple et double moment qui contient cinq variables pronostiques est présentement implémenté dans le modèle GEM. Cette analyse devrait être refaite afin de déterminer la valeur ajoutée de ce schéma microphysique plus complexe en parrallèle avec des tests sur de plus courtes périodes. Les simulations de courtes durées permettront de vérifier les effets directs (sans rétroaction) sur la simulation des nuages, de leurs propriétés radiatives et de leur production de précipitation, alors que l'analyse sur de plus longues périodes simulées telle que présentée dans ce mémoire, permettra d'évaluer les rétroactions des nuages dans le système climatique.

Il est à noter que certaines limites de cette étude résident dans l'incertitude des observations et leur disponibilité dans le temps. Comme il est mentionné dans la section 2c de l'article, les observations de la fraction nuageuse sont les plus problématiques quant à leurs incertitudes puisqu'en comparant jusqu'à cinq sources d'observations indépendantes, d'importantes différences ont pu être notées. Parmi ces différentes sources d'observations, certaines résultent d'un travail combinant plusieurs instruments et d'une analyse plus approfondie pour corriger certains biais provenant des instruments ou des algorithmes qui produisent les données utilisées, comme les produits *MICROBASE* et

LONG. Ces données semblent plus fiables que les données directement extraites d'un seul instrument d'observations, mais leur disponibilité dans le temps est limitée aux années plus récentes de la période étudiée. C'est pour cette raison qu'il a été décidé de prendre les observations concordant le plus entre elles, incluant les produits plus élaborés, et de les moyenner lorsqu'elles sont disponibles, pour ensuite les comparer avec la fraction nuageuse modélisée. Malgré cet effort, la fraction nuageuse observée reste entachée d'une incertitude d'environ 15 %. Pour les observations de vapeur d'eau et d'eau liquide, elles proviennent d'un produit élaboré à l'aide de plusieurs instruments de mesures et offre une incertitude relativement basse (≈ 18 g m^{-2} pour l'eau liquide et ≈ 0.7 kg m^{-2} pour la vapeur d'eau) par rapport aux produits habituellement utilisés dans des études similaires (25 g m^{-2} pour l'eau liquide, van Meijgaard et Crewell (2005)). Cependant, elles ne sont disponibles que pour quelques années au site NSA et cela mène à des statistiques moins robustes lorsque comparées avec les variables du modèle. Toutefois, ce produit est appliqué régulièrement à de nouvelles périodes et offrira bientôt la possibilité de vérifier les résultats obtenus au site NSA sur de plus longues périodes. De plus, les observations de l'eau solide des nuages ne semblaient pas de qualité suffisante pour être utilisables au moment de l'étude et un suivi devrait être fait à ce niveau puisque cette quantité permettrait d'éclaircir certains biais et de compléter l'analyse de l'interaction entre le contenu en eau total (et la séparation en eau liquide et solide) des nuages et le rayonnement. Finalement, les observations satellitaires sont en constante amélioration et incluent de plus en plus d'informations sur le contenu en eau de l'atmosphère. Ces sources d'observations devraient être exploitées afin de corroborer les observations déjà utilisées et surtout pour élargir le spectre de conditions atmosphériques comparables entre les observations et les simulations.

Pour récapituler, cette étude illustre l'importance de l'évaluation individuelle des composantes de l'interaction nuage-rayonnement afin de bien identifier les erreurs compensatoires qui peuvent être présentes. En outre, pour améliorer le bilan radiatif de surface de GEM-LAM, les principaux biais à améliorer sont la fraction nuageuse, l'interaction des nuages optiquement minces avec le rayonnement, la production de la précipitation

et l'influence des aérosols sur les processus microphysiques et radiatifs des nuages. Ce type d'évaluation est important dans le contexte des projections climatiques pour s'assurer que les modèles climatiques ont la capacité de reproduire les diverses rétroactions des nuages sur le système climatique pour des conditions climatiques changeantes ou du moins pour quantifier leur incertitude dans ce domaine alors qu'il est aussi important pour les modèles de prévision pour mieux identifier l'origine des biais radiatifs et ainsi pouvoir les corriger.

Bibliographie

Bélair, S., R. Brown, J. Mailhot, B. Bilodeau, et L.-P. Crevier. 2003a. « Operational implementation of the ISBA land surface scheme in the Canadian regional weather forecast model. Part II : Cold season results », *J. Hydrometeor.*, vol. 4, p. 371–386.

Bélair, S., L.-P. Crevier, J. Mailhot, B. Bilodeau, et Y. Delage. 2003b. « Operational implementation of the ISBA land surface scheme in the Canadian regional weather forecast model. Part I : Warm season results », *J. Hydrometeor.*, vol. 4, p. 352–370.

Bélair, S., J. Mailhot, C. Girard, et P. Vaillancourt. 2005. « Boundary layer and shallow cumulus clouds in a medium-range forecast of a large-scale weather system », *Mon. Wea. Rev.*, vol. 133, p. 1938–1960.

Bélair, S., J. Mailhot, J. W. Strapp, et J. I. MacPherson. 1999. « An examination of local versus nonlocal aspects of a TKE-based boundary layer scheme in clear convective conditions », *J. Appl. Meteor.*, vol. 38, p. 1499–1518.

Bony, S. et J.-L. Dufresne. 2005. « Marine boundary layer clouds at the heart of tropical cloud feedback uncertainties in climate models », *Geophys. Res. Lett.*, vol. 32.

Bougeault, P. et P. Lacarrère. 1989. « Parameterization of orography-induced turbulence in a mesobeta-scale model », *Mon. Wea. Rev.*, vol. 117, p. 1872–1890.

Cess, R. D. et Coauthors. 1996. « Cloud feedback in atmospheric general circulation models : An update », *J. Geophys. Res.*, vol. 101, p. 12791–12794.

Chen, B., J. Kasher, J. Maloney, A. Girgis, et D. Clark. 1991. « Determination of the clear sky emissivity for use in cool storage roof and roof pond applications ». In *ASES Proc.* Denver, CO.

Côté, J., S. Gravel, A. Méhot, A. Patoine, M. Roch, et A. Staniforth. 1998. « The operational CMC-MRB Global Environmental Multiscale (GEM) Model. Part I : Design considerations and formulation », *Mon. Wea. Rev.*, vol. 126, p. 1373–1395.

Curry, J. A. et Coauthors. 2000. « FIRE Arctic clouds experiment », *Bull. Amer. Meteor. Soc.*, vol. 81, p. 5–29.

Curry, J. A., W. B. Rossow, D. Randall, et J. L. Schramm. 1996. « Overview of Arctic cloud and radiation characteristics », *J. Climate*, vol. 9, p. 1731–1764.

Hogan, R. J., C. Jakob, et A. J. Illingworth. 2001. « Comparison of ECMWF winter-season cloud fraction with radar-derived values », *J. Appl. Meteor.*, vol. 40, p. 513–525.

Iacobellis, S. F., G. M. McFarquhar, D. L. Mitchell, et R. C. J. Somerville. 2003. « The sensitivity of radiative fluxes to parameterized cloud microphysics », *J. Climate*, vol. 16, p. 2979–2996.

Intrieri, J. M., M. D. Shupe, T. Uttal, et B. J. McCarty. 2002. « A annual cycle of Arctic cloud characteristics observed by radar and lidar at SHEBA », *J. Geophys. Res.*, vol. 107, p. 5–1–5–15.

Kain, J. et J. M. Fritsch. 1990. « A one-dimensional entraining/detraining plume model and its application in convective parameterization », *J. Atmos. Sci.*, vol. 47, p. 2784–2802.

———. 1993. « Convective parameterization for mesoscale models : The Kain-Fritsch scheme. », *The Representation of Cumulus Convection in Numerical Models, Meteor. Monogr. Amer. Meteor. Soc.*, vol. 46, p. 165–170.

Karlsson, K.-G., U. Willén, C. Jones, et K. Wyser. 2008. « Evaluation of regional cloud climate simulations over Scandinavia using a 10-year NOAA Advanced Very High Resolution Radiometer cloud climatology », *J. Geophys. Res.*, vol. 113.

Kassianov, E., C. N. Long, et M. Ovtchinnikov. 2005. « Cloud sky cover versus cloud fraction : Whole-sky simulations and observations », *J. Appl. Meteor.*, vol. 44, p. 86–98.

Key, J. et R. G. Barry. 1989. « Cloud cover analysis with Arctic AVHRR data : 1. Cloud detection », *J. Geophys. Res.*, vol. 94, p. 18521–18535.

Kong, F. et M. K. Yau. 1997. « An explicit approach to microphysics in MC2 », *Atmos. Ocean*, vol. 35, p. 257–291.

Lenderink, G., A. P. Siebesma, S. Cheinet, S. Irons, C. G. Jones, P. Marquet, F. Müller, D. Olmeda, J. Calvo, E. Sánchez, et P. M. M. Soares. 2004. « The diurnal cycle of shallow cumulus cloud over land : A single-column model intercomparison study », *Quart. J. Roy. Meteor. Soc.*, vol. 130, p. 3339–3364.

Li, J. et W. Barker. 2005. « A radiation algorith with correlated-k distribution. Part I : Local thermal equilibrium », *J. Atmos. Sci.*, vol. 62, p. 286–309.

Liou, K. N. 1992. *Radiation and cloud processes in the atmosphere : theory, observation and modeling.* Oxford University Press.

Lohman, U. et E. Roeckner. 1996. « Design and performance of a new cloud microphysics scheme developed for the echam general circulation model », *Climate Dyn.*, vol. 12, p. 557–572.

Long, C. N., T. P. Ackerman, J. J. DeLuisi, et J. A. Augustine. 1999. « Estimation of fractional sky cover from broadband SW radiometer measurements ». In *Proc. 10th Conf. on Atmos. Rad.* Madison, WI, Amer. Meteor. Soc.

Lonnqvist, J. 1995. « Experience with a novel single-lens cloud height lidar. ». In *Preprints, 9th Symp. on Meteor. Obs. and Instrum.*, p. 106–109. Charlotte, NC, Amer. Meteor. Soc.

Lucas-Picher, P., D. Caya, S. Biner, et R. Laprise. 2008. « Quantification of the lateral boundary forcing of a regional climate model using ageing tracer », *Mon. Wea. Rev.*

Markovic, M., C. G. Jones, P. A. Vaillancourt, D. Paquin, K. Winger, et D. Paquin-Ricard. 2008. « An evalution of the surface radiation budget over north america for a suite of regional climate models against surface station observations », *Climate Dyn.*, vol. 31, p. 779–794.

Martin, G. M., M. A. Ringer, V. D. Pope, A. Jones, C. Dearden, et T. J. Hinton. 2006. « The physical properties of the atmosphere in the new Hadley Centre Global Environmental Model (HadGEM1). Part I : Model description and global climatology », *J. Climate*, vol. 19, p. 1274–1301.

Meinke, I. 2006. « A comparison of simulated clouds to ISCCP data », *Mon. Wea. Rev.*, vol. 134, p. 1669–1681.

Milbrandt, J. A. et M. K. Yau. 2005a. « A multimoment bulk microphysics parameterization. Part I : Analysis of the role of the spectral shape parameter », *J. Atmos. Sci.*, vol. 62, p. 3051–3064.

———. 2005b. « A multimoment bulk microphysics parameterization. Part II : A proposed three-moment closure and scheme description », *J. Atmos. Sci.*, vol. 62, p. 3065–3081.

Miller, M., K. Johnson, P. Michael, et G. Mace. 2005. « MICROBASE, a continuous baseline microphysical retrieval : Status and future plans ». In *Proc. 15th ARM Science Team Meeting*. Daytona Beach, FL, Atmos. Rad. Meas.

Morrison, H., J. A. Curry, et V. I. Khvorostyanov. 2005a. « A new double-moment microphysics parameterization for application in cloud and climate models. Part I : Description », *J. Atmos. Sci.*, vol. 62, p. 1665–1677.

Morrison, H., J. A. Curry, M. D. Shupe, et P. Zuidema. 2005b. « A new double-moment microphysics parameterization for application in cloud and climate models. Part II : Single-column modeling of Arctic clouds », *J. Atmos. Sci.*, vol. 62, p. 1678–1692.

Morrison, H. et J. O. Pinto. 2006. « Intercomparison of bulk cloud microphysics scheme in mesoscale simulations of springtime Arctic mixed-phase stratiform clouds », *Mon. Wea. Rev.*, vol. 134, p. 1880–1900.

Norris, J. R. et C. P. Weaver. 2001. « Improved techniques for evaluating GCM cloudiness applied to the NCAR CCM3 », *J. Climate*, vol. 14, p. 2540–2550.

Randall, D. A., R. A. Wood, S. Bony, R. Colman, T. Fichefet, J. Fyfe, V. Kattsov, A. Pit-

man, J. Shukla, J. Srinivasan, R. J. Stouffer, A. Sumi, et K. E. Taylor. 2007. *Climate Models and Their Evaluation. Chapter 8 in : Climate Change 2007 : The Physical Science Basis. Contribution of Working Group I to the Fourth Assessment Report of the Intergovernmental Panel on Climate Change.* Cambridge University Press.

Roads, J., S. Chen, S. Cocke, L. Druyan, M. Fulakeza, T. LaRow, P. Lonergan, J.-H. Qian, et S. Zebiak. 2003. « International research institute/applied research centers (IRI/ARCs) regional model intercomparison over South America », *J. Geophys. Res.*, vol. 108, p. 9–1–9–12.

Rockel, B., E. Raschke, et B. Weyres. 1991. « A parameterization of broad band radiative transfer properties of water, ice, and mixed clouds », *Beitr. Phys. Atmos.*, vol. 64, p. 1–12.

Rossow, W. B. et R. A. Schiffer. 1991. « ISCCP cloud data products », *Bull. Amer. Meteor. Soc.*, vol. 72, p. 2–20.

———. 1999. « Advances in understanding clouds from ISCCP », *Bull. Amer. Meteor. Soc.*, vol. 80, p. 2261–2287.

Schweiger, A. J. et J. R. Key. 1992. « Arctic cloudiness : Comparison of ISCCP-C2 and Nimbus-7 satellite-derived cloud products with a surface-based cloud climatology », *J. Climate*, vol. 5, p. 1514–1527.

Shi, Y. et C. N. Long. 2002. « Techniques and methods used to determine the best estimate of radiation fluxes at SGP central facility ». In *Twelfth ARM Science Meeting Proc.* St. Petersburg, FL, Atmos. Rad. Meas.

Shupe, M. D., S. Y. Matrosov, et T. Uttal. 2006. « Arctic mixed-phase cloud properties derived from surface-based sensors at SHEBA », *J. Atmos. Sci.*, vol. 63, p. 697–711.

Shupe, M. D., T. Uttal, et S. Y. Matrosov. 2005. « Arctic cloud microphysics retrievals from surface-based remote sensors at SHEBA », *J. Appl. Meteor.*, vol. 44, p. 1544–1562.

Soden, A. et Held. 2006. « An assessment of climate feedbacks in coupled ocean-atmosphere models », *J. Climate*, vol. 19, p. 3354–3360.

Stephens, G. L. 2005. « Cloud feedbacks in the climate system : A critical review », *J. Climate*, vol. 18, p. 237–273.

Stephens, G. L. et P. J. Webster. 1981. « Clouds and climate : Sensitivity of simple systems », *J. Atmos. Sci.*, vol. 38, p. 235–247.

Sundqvist, H. 1988. « Parameterization of condensation and associated clouds in models for weather prediction and general circulation simulation », *Physically-Based Modelling and Simulation of Climate and Climatic Change - Part 1, NATO-ASI Series, Series C : Math. and Phys. Sciences*, vol. 243, p. 433–461.

Swinbank, W. C. 1963. « Long-wave radiation from clear skies », *Quart. J. Roy. Meteor. Soc.*, vol. 89, p. 339–348.

Tjernström, M., J. Sedlar, et M. D. Shupe. 2008. « How well do regional climate models reproduce radiation and clous in the Arctic ? An evaluation of ARCMIP simulations », *J. Climate Appl. Meteor.*

Toon, O. B. et J. B. Pollack. 1976. « A global average model of atmospheric aerosols for radiative transfer calculations », *J. Appl. Meteor.*, vol. 15, p. 225–246.

Turner, D. D., S. A. Clough, J. C. Liljegren, E. E. Clothiaux, K. E. Cady-Pereira, et K. L. Gaustad. 2007. « Retrieving liquid water path and precipitable water vapor from the atmospheric radiation measurement (ARM) microwave radiometers », *IEEE Trans. Geosci. Remote Sens.*, vol. 45, p. 3680–3690.

Uppala, S. M., P. W. K. Ilberg, A. J. Simmons, U. Andrae, V. da Costa Bechtold, M. Fiorino, J. K. Gibson, J. Haseler, A. Hernandez, G. A. Kelly, X. Li, K. Onogi, S. Saarinen, N. Sokka, R. P. Allan, E. Andersson, K. Arpe, M. A. Balmaseda, A. C. M. Beljaars, L. van de Berg, J. Bidlot, N. Bormann, S. Caires, F. Chevallier, A. Dethof, M. Dragosavac, M. Fisher, M. Fuentes, S. Hagemann, E. Hólm, B. J. Hoskins, L. Isaksen, P. A. E. M. Janssen, R. Jenne, A. P. McNally, J.-F. Mahfouf, J.-J. Morcrette, N. A. Rayner, R. W. Saunders, P. Simon, A. Sterl,

K. E. Trenberth, A. Untch, D. Vasiljevic, P. Viterbo, et J. Woollen. 2005. « The era-40 re-analysis », *Quart. J. R. Meteorol. Soc.*, vol. 131, p. 2961–3012.

van Meijgaard, E. et S. Crewell. 2005. « Comparison of model predicted liquid water path with ground-based measurments during CLIWA-NET », *Atmos. Res.*, vol. 75, p. 201–226.

Walsh, J. E., V. M. Kattsov, W. L. Chapman, V. Govorkova, et T. Pavlova. 2002. « Comparison of arctic climate simulations by uncoupled and coupled global models », *J. Climate*, vol. 15, p. 1429–1446.

Weare, B. C. 2004. « A comparison of AMIP II model cloud layer properties with ISCCP D2 estimates », *Climate Dyn.*, vol. 22, p. 281–292.

Welton, E. J. et J. R. Campbell. 2002. « Micropulse lidar signals : Uncertainty analysis », *J. Atmos. Oceanic Technol.*, vol. 19, p. 2089–2094.

Willén, U., S. Crewell, H. K. Baltink, et O. Sievers. 2005. « Assessing model predicted vertical cloud structure and cloud overlap with radar and lidar ceilometer observations for the Baltex Bridge Campaign of CLIWA-NET », *Atmos. Res.*, vol. 75, p. 227–255.

Williams, K. D., M. A. Ringer, C. A. Senior, M. J. Webb, B. J. McAvaney, N. Andronova, J.-L. D. S. Bony, S. Emori, R. Gudgel, T. Knuston, B. Li, K. Lo, I. Musat, J. Wegner, A. Slingo, et J. F. B. Mitchell. 2006. « Evaluation of a component of the cloud response to climate change in an intercomparison of climate models », *Climate Dyn.*, vol. 26, p. 145–165.

Wyser, K. et C. G. Jones. 2005. « Modeled and observed clouds during surface heat budget of the Arctic Ocean (SHEBA) », *J. Geophys. Res.*, vol. 110, p. 1–9.

Wyser, K., C. G. Jones, P. Du, E. Girard, U. Willén, J. Cassano, J. H. Christensen, J. A. Curry, K. Dethloff, J.-E. Haugen, D. Jacob, M. Koltzov, R. Laprise, A. Lynch, S. Pfeifer, A. Rinke, M. Serreze, M. J. Shaw, M. Tjernström, et M. Zagar. 2008. « An evaluation of Arctic cloud and radiation processes during the SHEBA year :

Simulation results from 8 Arctic regional climate models », *Climate Dyn.*, vol. 30, p. 203–223.

Yuan, J., Q. Fu, et N. McFarlane. 2006. « Tests and improvements of GCM cloud parameterizations using the CCCMA SCM with the SHEBA data set », *Atmos. Res.*, vol. 82, p. 222–238.

Zadra, A., D. Caya, J. Côté, B. Dugas, C. Jones, R. Laprise, K. Winger, et L.-P. Caron. 2008. « The next Canadian regional climate model », *Phys. Canada*, vol. 64, p. 74–83.